Marine and Petroleum Geology 160 (2024) 106626

Contents lists available at ScienceDirect

Marine and Petroleum Geology

journal homepage: www.elsevier.com/locate/marpetgeo

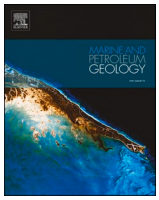

The mechanism of organic matter accumulation in the archipelago marine sediments: Insights from the Middle Devonian Givetian mudstone with low TOC in the Youjiang Basin, South China

Yuzuo Liu [a,b,c], Wanzhong Shi [a,b,*], Qinhong Hu [d], Kun Yuan [e,f], Xiaofeng Xu [a,b], Xiaoming Zhang [a,b], Ren Wang [a,b], Xianglin Chen [e], Luheng Bai [a,b], Murray K. Gingras [c], Kurt O. Konhauser [c]

[a] Key Laboratory of Tectonics and Petroleum Resources of Ministry of Education, China University of Geosciences, Wuhan, 430074, China
[b] School of Earth Resources, China University of Geosciences, Wuhan, 430074, China
[c] Department of Earth and Atmospheric Sciences, University of Alberta, Edmonton, Alberta, T6G 2E3, Canada
[d] Department of Earth and Environmental Sciences, The University of Texas at Arlington, Arlington, TX, 76019, USA
[e] Oil and Gas Survey Center, China Geological Survey, Beijing, 100029, China
[f] School of Energy Resources, China University of Geosciences, Beijing, 100083, China

ARTICLE INFO

Keywords:
Element geochemistry
Paleoenvironmental condition
Organic matter accumulation mechanism
Archipelagic marine
Middle Devonian
The Youjiang basin

ABSTRACT

Despite the fact that the mean values of total organic carbon (TOC) content in the Luofu Formation are relatively low, at or below 1.0 wt%, it still has the potential to be a veritable source rock. To elucidate the influences of various paleogeographic factors on sedimentary environments, 25 samples from Well A on the slope and 32 samples from Well B in the basin centre were selected for study. The samples were analyzed by thin section microscopy and field emission-scanning electron microscopy, along with X-ray diffraction and geochemical analyses (TOC content, sulfur content, organic petrography, inorganic carbon isotope and major and trace elements) in order to understand variations in and controls on the mineralogy, lithofacies, depositional environments, as well as the organic matter accumulation mechanism. The results of our study indicate that mudstone of the Luofu Formation was deposited into 4 lithofacies groups, namely as the siliceous lithofacies, mixed lithofacies, argillaceous lithofacies and calcareous lithofacies. The siliceous lithofacies mudstone was developed in the deep-water columns, while the mixed lithofacies mudstone was deposited on shallow-water columns. The organic matter accumulation model of the Luofu Formation can be further divided into the following four stages, each with its own unique characteristics: (1) The organic matter accumulation was caused by the relatively high productivity and dysoxic basin bottom water columns; (2) The organo-mineral complexes may promote the organic matter accumulation to some extent; (3) The organic matter enrichment was facilitated by the dysoxic/anoxic conditions and relatively high productivity from the basin to the slope; (4) The organic matter was preserved at shortened exposure duration of oxic conditions on the slope. The correlations between various geochemical indicators (redox, paleoproductivity and terrestrial debris flux) and TOC content suggest that oxic water columns and low productivity are the main reasons for the widespread mudstone with low TOC. The organic-rich mudstone, as the target stratigraphic section for exploration, may be deposited in the basin bottom water columns away from upwelling and close to hydrothermal activity in stage 3.

1. Introduction

China has witnessed breakthroughs in shale gas exploration and production, particularly in the regions of Fuling in Chongqing and Weiyuan in Sichuan (Zou et al., 2019, 2023; Qiu et al., 2022). Previous studies have sought to elucidate the processes governing the accumulation and preservation of organic matter in the deep-water shelf shale (Yan et al., 2018; Wu et al., 2019; Tang et al., 2020; Xiao et al., 2021). The Luofu Formation mudstone was deposited around 387.7 to 382.7 Ma in a shallow-water shelf setting of the Youjiang Basin in south China.

* Corresponding author. Key Laboratory of Tectonics and Petroleum Resources of Ministry of Education, China University of Geosciences, Wuhan, 430074, China.
E-mail address: shiwz@cug.edu.cn (W. Shi).

https://doi.org/10.1016/j.marpetgeo.2023.106626
Received 2 August 2023; Received in revised form 16 November 2023; Accepted 23 November 2023
Available online 30 November 2023

This mudstone accumulated in a range of sedimentary environments due to the influence of global sea-level fluctuations and the presence of an archipelago characterized by multiple islands (Fig. 1a) (Wu et al., 2022). It is worth noting that, the study area demonstrates exceptional potential for marine-sourced oil and gas, supported by the exploration findings of conventional oil and gas reservoirs (Cheng, 2011a; Yang et al., 2020). But so far, the reasons behind the dissimilar organic matter accumulation in the Luofu Formation mudstone remain unknown (Du et al., 2009; Yuan et al., 2020). This limits the assessment of mudstone shale-associated petroleum potential and the understanding of regional petroleum source rocks.

The organic matter concentration in marine mudstone is determined by several factors, including biological productivity, preservation conditions, and sedimentation rates. Depending on the relative importance of these factors, two different preservation and productivity models have been established (Calvert and Pederson, 1992; Tyson, 1995; Yuan et al., 2020; Teng et al., 2021). The first model focuses on the preservation of organic matter resulting from anoxic water column conditions.

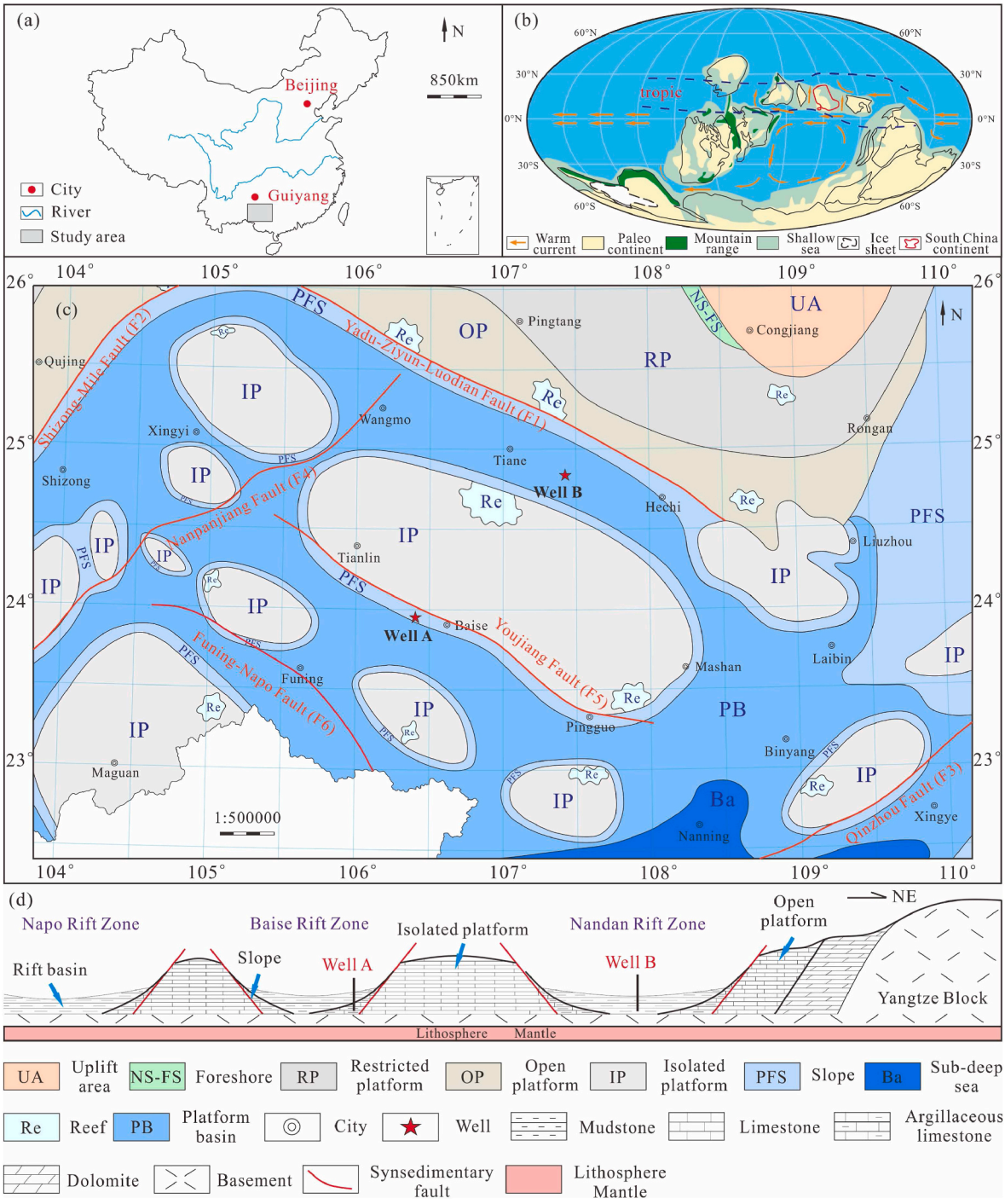

Fig. 1. (a) Location of the study area in China (modified from Zhang et al., 2019); (b) Global paleogeography (modified from Scotese and McKerrow, 1990; Golonka, 2002) and paleoclimatic reconstructions of the Middle Devonian (Paleoclimatic reconstructions from Zhang et al., 2019. Ocean current from Scotese, 2001); (c) Palaeogeographic map showing the distribution of sedimentary facies and locations of sampling Well A and Well B (modified from Ma et al., 2009; Chen et al., 2010; Mei et al., 2013); (d) Sedimentary structure section showing the characteristics of lithofacies paleogeography in Well A and Well B (modified from Cheng, 2011b).

The second model considers elevated paleoproductivity rates as the more important variable (Ross and Bustin, 2009; Ma et al., 2016; Sweere et al., 2016; Wang et al., 2019). The amount of total organic carbon (TOC) preserved can also be influenced by post-depositional processes such as hydrocarbon generation and thermal maturation (Zhong et al., 2004).

For instance, Yuan et al. (2020) proposed a redox-dominated organic matter accumulation model for the Luofu Formation mudstone through longitudinal variations in drilling geochemical indicators. However, the shallow-water archipelagic marine environments are more complex than deep-water shelf settings, likely due to the impact of terrestrial material (Yang et al., 2020). Therefore, this model does not explain the extensive development of organic-poor mudstone deposited in anoxic water columns during the Givetian stage. Additionally, it should be emphasized that mudstone with low TOC content has been deposited in the shallow-water archipelagic marine environments, including the Middle Devonian Xiangzhong Depression, the Late Permian northeastern Sichuan Basin (Chen et al., 2010; Wu et al., 2019), the Late Ordovician Tarim Basin (Xiao et al., 2021), the Appalachian Basin of North America, and the Upper Devonian Western Canada Basin (Chabalala et al., 2020). These occurrences underscore the importance of determining the appropriate organic matter accumulation model for this specific sedimentary environment.

To clarify the influence of an archipelagic marine paleogeographic environment on the mechanism of organic matter accumulation, a total of 25 samples representing the slope strata from Well A and 32 samples representing the basin strata from Well B were chosen. Samples were analyzed by thin section microscopy and field emission-scanning electron microscopy, along with X-ray diffraction and geochemical analyses (TOC content, sulfur content, organic petrography, inorganic carbon isotope and major and trace elements) to identify and quantify the variations in redox condition, paleoproductivity, detrital influx, and mineral compositions. The study was carried out with specific objectives in mind: (1) to identify the variations in the distribution of organic-rich and organic-poor mudstone; (2) to explain the factors that govern organic-poor mudstone; (3) to clarify the processes of organic matter accumulation during the deposition of mudstone sedimentary facies; and (4) to propose a model for the accumulation of organic matter in an archipelagic marine setting. The findings of this study are anticipated to serve as a guide for analyzing the spatial and temporal variations of hydrocarbon source rocks in basins characterized by an archipelagic marine environment, such as the Youjiang Basin.

2. Geological setting

The Youjiang Basin, located at the junctions of Southeast Yunnan, Western Guangxi, and Southern Guizhou, is part of the South China Plate (Fig. 1a) (Wang and Groves, 2018; Yang et al., 2023). It is also located at the intersection of Paleo-Tethys and Paleo-Pacific tectonic domains. Both the Youjiang Basin and the Paleo-Tethys Ocean have expanded since the Devonian, leading to fault development in the basin. The Yadu-Ziyun-Luodian Fault (F1) is the boundary in the North, the Shizong-Mile Fault (F2) is the boundary in the West, and the Qinzhou Fault (F3) is the boundary in the East (Mei et al., 2007; Yang et al., 2020). During the Givetian Stage, the Youjiang Basin was located at low latitudes and the climate was tropical to sub-tropical (Fig. 1b) (Qie et al., 2019).

During the Early Devonian Period, the activity along the Shizong-Mile Fault (F2) and the Nanpanjiang Fault (F4) resulted in many aulacogens showing a NE trend. The later formation of the Yadu-Ziyun-Luodian Fault (F1), the Youjiang Fault (F5), and the Guangnan-Funing-Napo Fault (F6) subsequently led to the northwest-trending deep-water rift troughs on the shallow shelves (Yu et al., 2018). During the late Early Devonian Period, an archipelagic marine paleogeographic pattern emerged, characterized by the presence of intersecting deep and shallow aulacogens, as well as alternating basins and platforms. As the transgression advanced from the southwest to the northeast, the Youjiang Basin became entirely submerged by seawater (Fig. 1c) (Huang et al., 2020; Shao et al., 2020).

Well A is located in Basie City, and Well B is in Hechi City, both in Guangxi Province (Fig. 1a, 1c-d). Well A of the Luofu Formation on the slope, calcareous mudstone was deposited in the lower and middle part, and argillaceous limestone and limestone are preserved in the upper part (Fig. 2a). Well B of the Luofu Formation is from the deeper basin. In this well, carbonaceous mudstone and mudstone were deposited in the lower section, a thick calcareous mudstone unit was deposited in the middle, and the upper strata comprised mudstone, siliceous mudstone and argillaceous limestone (Fig. 2b). At the platform edge of the Luofu Formation, reefs were established, and the platform accumulated carbonate and bioclastic limestone (Fig. 1d) (Fan et al., 2004; Cheng, 2011a; Mei et al., 2013).

3. Samples and methods

3.1. Core samples

To identify the influences of paleogeographic patterns on the Luofu Formation sedimentary environments, a thorough examination of core samples was carried out from Well A located on the slope, as well as Well B situated within the basin. A total of 25 samples from Well A and 32 samples from Well B were collected for X-ray diffraction (XRD), thin section optical microscopy and Field Emission-Scanning Electron Microscopy (FE-SEM) to reflect the petrologic and mineral characteristics of the Luofu Formation (Fig. 2). These samples were selected for further analysis of TOC content, sulfur content, organic matter source tracking and major and trace elements. Furthermore, to gain insights into relative sea-level fluctuations, samples extracted from Well An underwent Inorganic Carbon Isotope ($\delta^{13}C_{carb}$) analyses. It is crucial to emphasize that all core samples were in a pristine state prior to examination, guaranteeing the veracity of the test outcomes in portraying the sedimentary conditions of the Luofu Formation.

3.2. X-ray diffraction (XRD), thin section optical microscopy and field emission-scanning electron microscopy (FE-SEM)

The samples were ground to less than 200 mesh for XRD, total organic carbon (TOC), and sulfur content analyses. The mineral composition was analyzed by XRD using a Smart Lab SE. Each sample was analyzed in duplicate by the Chinese Industry-Standard SY/T 5163–2018.

A Leica DM4500P microscope was used to observe thin sections (cut perpendicular to bedding) for determining the mineral and lamellar morphology and paleontological traces. The instrument IM4000 was used for polishing samples and Hitachi S-8000 was used for FE-SEM. The images of microscopy and SEM for each sample were taken at multiple locations by the Chinese Industry-Standard SY/T 5162–2014.

3.3. TOC content, sulfur content, and inorganic carbon isotopes

For TOC and sulfur content, the samples were analyzed by Leco CS-230 Carbon and Sulfur Analyzer. The analyses were carried out in accordance with the Chinese National-Standard GB/T 19145–2003. The accuracy was better than 0.2%.

GasBench II carbonate device and MAT253 online test were used for the inorganic carbon isotope test. Firstly, a sample of 50 μg was placed into a 12 ml reaction flask and sealed it with an insulating pad. By moving the emptying needle in sequence, the reaction bottles were rinsed to eliminate the influence of air in the bottle on the test results. Then 0.14 ml of 99% phosphoric acid was added into the reaction flask with acid needle and acid pump. The carbon dioxide produced by the reaction of phosphoric acid and samples were driven by helium to remove water. Finally, carbon dioxides were separated from other

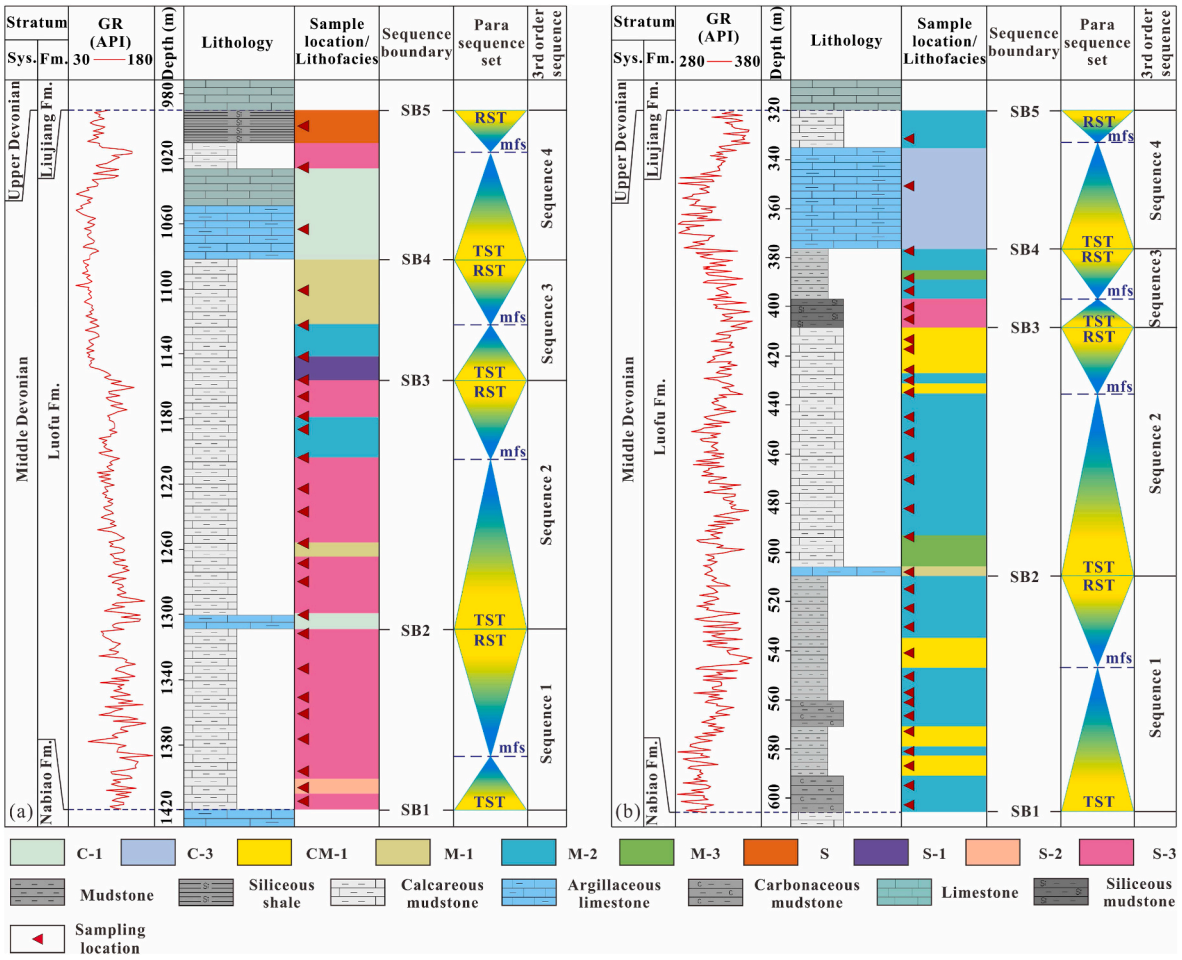

Fig. 2. Lithology, lithofacies, GR logging, and sedimentary structures of Well A (a) and Well B (b). Each lithofacies code (C-2 et al.) refers to Fig. 3. The sequence framework of the Luofu Formation on the basis of previous sequence division results (Du et al., 1996, 1997, 2009; Gong and Wu, 1997; Gong et al., 1994; Gradstein, 2020), lithological characteristics and GR curve change points from Well A (a) and Well B (b).

impure gases by a 72 °C chromatographic column and entered a mass spectrometer to obtain carbon isotope values. International standard materials NBS18, NBS19, and LSVEC were used to calibrate the experimental equipment. According to the Chinese National-Standard SY/T 5238–2019, each sample was analyzed three times, and the accuracy of tests was better than 0.1 ‰.

3.4. Organic petrography

The Luofu Formation polished sections were observed via NIKON-LV100 microscope under reflected light at 500 times magnification (50× oil immersion objective) to study the petrographic features of the organic matter. The maceral compositions were identified according to the classification criteria for vitrinite (International Committee for Coal and Organic Petrology, 1998), liptinite (Pickel et al., 2017), and inertinite (International Committee for Coal and Organic Petrology, 2001). The identification of the Luofu Formation samples involved the use of a DM4500P polarized fluorescence microscope to analyze kerogen macerals through transmission-fluorescence techniques. The experimental process followed the Chinese Industry-Standard SY/T5125-2014.

3.5. Major and trace elements by X-ray fluorescence and inductively coupled plasma-mass spectrometry

The mesh samples were baked in an oven at 105 °C for 12 h to prepare the test of the whole rock major and trace element. About 1.2 g fresh samples are combusted in a muffle furnace at 1000 °C for 2 h. Subsequently, they were weighed to determine the ignition loss. Next, a mixture comprising the samples, cosolvent, and oxidant was heated until it reached a molten state and held there for 15 min. Lastly, the mixture was cooled down for the purpose of conducting an XRF test. After OM is completely removed, ~50 mg residual samples were acidified, and then heated for one day. Subsequently, a mixed solution containing HNO_3, MQ, and an internal standard was added to the samples and heated for a duration of half a day. Finally, the samples were diluted with HNO_3 in preparation for ICP-MS analysis. The major element analyses were conducted on XRF (Primus II), and the trace element analyses were carried out on Agilent 7700e ICP-MS at the Wuhan Sample Solution Analytical Technology Co., Ltd., Wuhan, China. Replicate analysis of samples and standard samples was used to calibrate the final results. Ensuring that the analytical error was less than 2%.

3.6. Data processing

Trace elements consist of both authigenic and terrestrial components, with only the authigenic components providing insights into the paleosedimentary environment (Tribovillard et al., 2006; Calvert and Pedersen, 2007). Titanium is considered a stable physical and chemical element in the rock terrestrial content. To eliminate the contribution of terrestrial detritus to elemental abundance, all of the elements are normalized to the titanium content (Xiao et al., 2021). The enrichment factor (X_{EF}) serves as a parameter that characterizes the degree of element enrichment and can additionally indicate the redox conditions during the deposition of mudstone (Tribovillard et al., 2006; Wang et al.,

2019) as the following equation:

$$X_{EF} = (X/Ti)_{sample} \Big/ (X/Ti)_{PAAS} \quad (1)$$

where X_{EF} is the enrichment factor of the element X, $(X/Ti)_{sample}$ is the ratio of element X to Ti measured in the sample, and $(X/Ti)_{PAAS}$ is the ratio of element X to Ti in the Post-Archean Australian Shale (PAAS) whose value was taken from Taylor and Mclennan (1985). $X_{EF} > 1.0$ indicates a state of element enrichment relative to the standard ratio (Tribovillard et al., 2012; Wang et al., 2019).

The degree of pyritization (DOP) is the ratio of iron in pyrite to total active iron (iron in pyrite and iron dissolved in hydrochloric acid) (Raiswell et al., 1988). Previous studies have shown that the ratio of iron total iron in pyrite is close to DOP, DOP_T can take the place of DOP (Raiswell and Berner, 1986). When estimating iron contents in pyrite, it is assumed that the sulfur is in the form of FeS_2 (Rimmer, 2004; Rowe et al., 2008). The value of DOP_T is calculated by the formula:

$$DOP_T = (55.85 / 64.16) \times S / Fe \quad (2)$$

where 55.85 and 64.16 are the atomic masses of Fe and S. S is the measured inorganic sulfur content and Fe is the content of total iron in a sample. When the sedimentary activity without magmatic activity, the contents of excess silicon and barium are approximately equal to those of biogenic silicon and barium, respectively. Biogenic silica (Si_{bio}) and

Table 1
XRD result of the Luofu Formation samples from Well A and Well B in the Youjiang Basin.

Stage	Depth/m	Well-Sample ID	Quartz/%	K-Feldspar/%	Plagioclase/%	Calcite/%	Dolomite/%	Siderite/%	Pyrite/%	Hematite/%	Anhydrite/%	Ankerite/%	Clay/%
4	999.30	A-1	73.20	1.60	1.10	0.00	4.20	0.70	1.70	0.90	0.60	0.00	16.00
4	1026.04	A-2	50.40	1.10	2.80	2.60	4.60	1.40	0.90	0.40	1.60	0.00	34.20
4	1063.60	A-3	31.80	0.10	0.30	51.90	3.70	0.00	0.80	0.40	3.80	0.00	7.20
3	1100.10	A-4	35.00	0.80	1.00	23.30	14.10	0.80	1.40	0.20	0.40	0.00	23.00
3	1121.60	A-5	46.00	0.50	1.40	3.50	17.40	0.40	2.40	0.40	0.90	0.00	27.10
3	1141.40	A-6	48.00	0.40	0.80	26.70	6.00	0.20	1.60	0.40	0.50	0.00	15.40
2	1154.40	A-7	49.60	0.70	0.70	0.60	0.00	0.70	1.30	0.50	0.90	14.50	30.50
2	1165.50	A-8	49.90	1.30	2.80	1.90	3.00	2.30	0.60	0.20	0.60	0.00	37.40
2	1178.40	A-9	58.80	1.10	2.20	0.50	0.00	0.30	0.40	0.00	0.70	0.00	36.00
2	1185.60	A-10	41.10	0.80	1.90	16.50	0.00	0.40	0.70	0.30	1.20	1.10	36.00
2	1203.60	A-11	52.20	0.70	2.50	4.30	1.40	1.20	0.90	0.50	0.70	0.00	35.60
2	1222.20	A-12	50.30	0.80	2.80	13.70	3.90	0.40	0.90	0.40	1.00	0.00	25.80
2	1235.90	A-13	47.60	1.00	2.40	7.00	2.10	0.40	0.90	0.40	0.00	0.00	38.20
2	1255.30	A-14	59.70	1.10	2.40	4.90	16.20	0.80	1.30	0.60	1.00	0.00	12.00
2	1267.90	A-15	52.50	1.20	2.30	2.10	0.80	1.20	0.60	0.30	1.10	0.00	37.90
2	1279.10	A-16	50.00	1.30	1.70	4.60	0.00	0.60	0.70	0.20	0.50	0.00	40.40
2	1298.40	A-17	30.50	1.50	2.50	50.60	4.40	0.00	0.20	0.20	1.60	0.00	8.50
1	1311.40	A-18	50.20	1.20	2.50	3.50	0.60	0.40	0.50	0.20	0.00	0.00	40.90
1	1332.20	A-19	51.20	0.50	3.30	9.40	0.30	1.10	0.70	0.30	1.00	0.00	32.20
1	1350.40	A-20	55.00	0.70	3.30	4.50	4.50	0.40	0.90	0.40	2.90	0.00	27.40
1	1361.15	A-21	44.20	0.90	2.60	11.70	7.30	0.80	1.10	0.60	3.30	0.00	27.50
1	1376.20	A-22	46.90	1.40	3.40	1.80	0.00	1.40	0.80	0.40	3.30	0.00	40.60
1	1396.40	A-23	66.40	0.80	2.40	1.50	0.80	1.10	1.10	0.30	0.80	0.00	24.80
1	1406.00	A-24	60.10	1.20	2.80	1.10	8.40	2.20	1.50	0.40	1.30	0.00	21.00
1	1414.60	A-25	56.20	1.10	2.50	5.60	7.60	0.60	0.60	0.20	1.40	0.00	24.20
4	331.50	B-1	39.00	0.00	2.00	4.00	5.00	1.00	5.00	0.10	1.00	0.00	43.00
4	350.10	B-2	13.00	0.00	2.00	45.00	4.00	1.00	5.00	0.20	1.00	0.00	29.00
3	377.30	B-3	39.00	1.00	2.00	5.00	4.00	1.00	2.00	0.10	1.00	0.00	45.00
3	390.10	B-4	32.00	0.00	1.00	17.00	10.00	1.00	2.00	0.10	1.00	0.00	36.00
3	393.30	B-5	41.00	1.00	2.00	3.00	2.00	2.00	3.00	0.20	1.00	0.00	45.00
3	401.30	B-6	49.00	1.00	2.00	6.00	2.00	1.00	1.00	0.30	1.00	0.00	37.00
3	402.90	B-7	49.00	0.00	1.00	1.00	4.00	2.00	2.00	0.10	1.00	0.00	40.00
2	415.70	B-8	32.00	1.00	2.00	1.00	4.00	2.00	2.00	0.10	1.90	1.00	53.00
2	417.30	B-9	29.00	0.00	3.00	2.00	9.00	2.00	2.00	0.10	1.90	0.00	51.00
2	426.90	B-10	28.00	1.00	3.00	2.00	10.00	1.00	2.00	0.20	1.80	0.00	51.00
2	431.10	B-11	36.00	1.00	2.00	2.00	8.00	0.00	2.00	0.20	0.80	0.00	48.00
2	435.30	B-12	37.00	1.00	2.00	2.00	4.00	2.00	2.00	0.20	1.80	0.00	48.00
2	444.90	B-13	35.00	1.00	2.00	1.00	10.00	2.00	2.00	0.10	0.90	0.00	46.00
2	451.30	B-14	38.00	1.00	2.00	3.00	6.00	2.00	3.00	0.10	1.90	0.00	43.00
2	467.30	B-15	42.00	0.00	2.00	2.00	4.00	1.00	2.00	0.20	0.80	0.00	46.00
2	468.90	B-16	38.00	0.00	2.00	4.00	8.00	2.00	3.00	0.20	0.80	0.00	42.00
2	476.90	B-17	41.00	1.00	2.00	2.00	2.00	2.00	2.00	0.10	0.90	0.00	47.00
2	493.10	B-18	27.00	0.00	2.00	2.00	30.00	2.00	1.00	0.20	0.80	0.00	35.00
2	509.20	B-19	45.00	0.00	2.00	27.00	3.00	1.00	1.00	0.10	0.90	0.00	20.00
1	518.70	B-20	30.00	0.00	2.00	3.00	18.00	2.00	1.00	0.20	1.80	0.00	42.00
1	525.10	B-21	36.00	1.00	3.00	6.00	8.00	2.00	2.00	0.10	1.90	0.00	40.00
1	526.70	B-22	30.00	1.00	3.00	9.00	12.00	2.00	2.00	0.10	1.90	0.00	39.00
1	541.10	B-23	32.00	1.00	3.00	4.00	4.00	1.00	3.00	0.30	1.70	0.00	50.00
1	550.70	B-24	37.00	0.00	3.00	5.00	4.00	2.00	2.00	0.10	1.90	0.00	45.00
1	557.10	B-25	34.00	1.00	2.00	3.00	8.00	2.00	2.00	0.20	0.80	0.00	47.00
1	558.70	B-26	35.00	0.00	2.00	9.00	6.00	1.00	1.00	0.20	0.80	0.00	45.00
1	566.70	B-27	38.00	0.00	2.00	12.00	2.00	1.00	3.00	0.10	0.90	0.00	41.00
1	573.10	B-28	31.00	1.00	2.00	3.00	4.00	2.00	2.00	0.10	0.90	0.00	54.00
1	581.10	B-29	43.00	1.00	2.00	2.00	3.00	2.00	3.00	0.20	1.80	0.00	42.00
1	587.10	B-30	32.00	1.00	3.00	3.00	7.00	2.00	3.00	0.20	1.80	0.00	47.00
1	595.10	B-31	31.00	0.00	2.00	17.00	5.00	2.00	2.00	0.10	0.90	0.00	40.00
1	603.10	B-32	42.00	1.00	2.00	3.00	5.00	1.00	2.00	0.10	0.90	0.00	43.00

biogenic barium (Ba_{bio}) are calculated as follows (Schoepfer et al., 2015):

$$Si_{bio} = [Si_{sample}] - [Ti_{sample} \times (Si/Ti)_{PAAS}] \quad (3)$$

$$Ba_{bio} = [Ba_{sample}] - [Ti_{sample} \times (Ba/Ti)_{PAAS}] \quad (4)$$

where Si_{sample}, Ti_{sample} and Ba_{sample} are the measured contents of elements Si, Ti and Ba in the mudstone samples, respectively. Values of $(Si/Ti)_{PAAS}$ and $(Ba/Ti)_{PAAS}$ are the ratios of Si/Ti and Ba/Ti in PAAS, respectively.

The classification of organic matter based on the relative content of microscopic fractions in kerogen can be determined by the value of TI (Zhong et al., 2004). The value of TI is calculated by the formula:

$$TI = \frac{a*(+100)+b*(+50)+c*(-75)+d*(-100)}{100} \quad (5)$$

where a, b, c, and d are the relative contents of sapropelinite, exinite, vitrinite, and inertinite, respectively. TI < 0 indicates kerogen type III, 0 < TI < 40 indicates kerogen type II_2, 40 < TI < 80 indicates kerogen type II_1, and 80 < TI < 100 indicates kerogen type I.

4. Results

4.1. Mineral components and lithofacies

The Luofu Formation samples predominantly consist of silicates, clay, and carbonate minerals (as shown in Table 1). Quartz and feldspar are the main silicate minerals; calcite and dolomite represent the principal carbonate minerals, and illite and kaolinite are the main clay minerals. The silicate mineral content is notably higher in Well A, ranging from 32.20% to 75.90% with an average of 53.40%, compared to that in Well B ranging from 15.00% to 52.00% with an average of 38.38%, while the clay mineral concentration is higher in Well B, ranging from 20.00% to 54.00% with an average of 43.13%, than that in Well A, ranging from 7.20% to 40.90% with an average of 27.99%.

From a stratigraphic perspective, in Well A, the silicate mineral content peaks in stage 1 (average = 57.60%), the clay mineral content is highest in stage 2 (average = 30.75%), and the carbonate mineral content tops in stage 3 (average = 30.33%). In Well B, the highest concentration of silicate minerals is in stage 2 (average = 55.80%), whereas stage 1 has the most significant amounts of clay (average = 44.23%) and stage 4 has the highest content of carbonate (average = 29.00%) mineral.

A ternary diagram plotting silicate, carbonate, and clay minerals (Ma et al., 2016; Wu et al., 2016) is shown in Fig. 3. Due to significant differences in mineral compositions, the samples are classified into 4 lithofacies groups and 10 lithofacies, including S, S-1, S-2, S-3, M-1, M-2, M-3, CM-1, C-1, C-3. The samples of Well A mainly belong to silicate-rich shale lithofacies and the samples of Well B are dominated by mixed lithofacies (Fig. 3). In Well A, clay-rich siliceous (S-3) shale was developed in stage 1 and stage 2 (Fig. 2). Calcareous mudstone is mainly clay-rich siliceous shale (S-3) and argillaceous limestone is mainly silica-rich calcareous shale (C-1) (Fig. 2). In Well B, argillaceous/siliceous mixed mudstone (M-2) was developed in mudstone of stages 1 and stage 3, and calcareous mudstone of stage 2 and 4. In stage 3, siliceous mudstone is clay-rich siliceous shale (S-3). In stage 4, limestone belongs to the clay-rich calcareous lithofacies (C-3) (Fig. 2).

4.2. Petrological characteristics

In stage 1 of the Luofu Formation, parallel bedding is developed with a large amount of bioclast (Fig. 4a–b). Along with the appearance of ripple cross laminated (Fig. 4b), many broken shells and calcite spherules are found in stage 2 (Fig. 4c–e). In stage 3, the parallel bedding of Well A (Fig. 4f) and the boundary between calcareous mudstone and siliceous mudstone of Well B (Fig. 4g) can be seen. In the calcareous mudstone, there are a large number of broken shells (Fig. 4h), calcite spherules (Fig. 4h), and terrigenous detrital particles with low structural maturity (Fig. 4i).

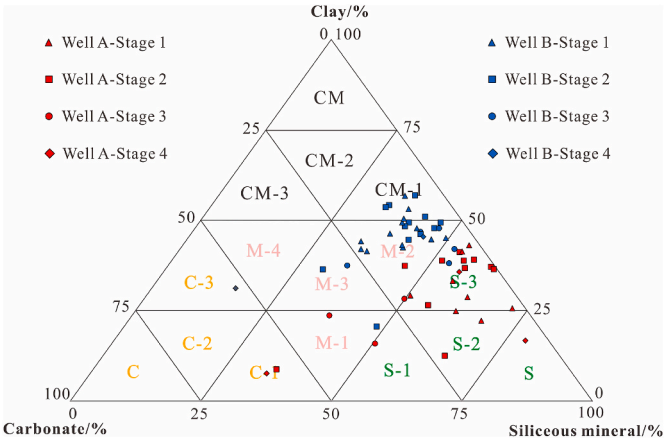

Fig. 3. Ternary diagram (modified from Ma et al., 2016; Wu et al., 2016) shows the mineralogical composition of nine major lithofacies in Well A and five major lithofacies in Well B. S: Siliceous shale lithofacies, S-1: Carbonate-rich siliceous shale lithofacies, S-2: Mixed siliceous shale lithofacies, S-3: Clay-rich siliceous shale lithofacies, M-1: Calcareous/siliceous mixed shale lithofacies, M-2: Argillaceous/siliceous mixed shale lithofacies, M-3: Mixed shale lithofacies, CM-1: Silica-rich argillaceous shale lithofacies, C-1: Silica-rich calcareous shale lithofacies, C-3: Clay-rich calcareous shale lithofacies.

4.3. Sequence stratigraphy

The core samples of the A and B wells were interpreted through the previous adapted sequence stratigraphic framework. Sequence Boundary #1: SB1 was identified due to the lithological differences between the Nabiao Formation and the overlying Luofu Formation (Figs. 2 and 5). Under SB1 interface, argillaceous mudstone was deposited in Well A and calcareous mudstone was deposited in Well B (Figs. 2, 5a and 5f). At interface of SB1, calcareous mudstone of S-3 in Well A and carbonaceous mudstone of M-2 in Well B were deposited in the Luofu Formation (Figs. 2, 5a and 5f). Sequence Boundary #2: SB2 was identified by the differences in lithology and lithofacies (Figs. 2 and 5). Under SB2 interface, calcareous mudstone of S-3 was in Well A and mudstone of M-2 was in Well B (Figs. 2, 5b and 5g). At interface of SB2, argillaceous mudstone of C-1 was deposited in Well A and calcareous mudstone of M-3 was deposited in Well B (Figs. 2, 5b and 5g). Sequence Boundary #3: SB3 was identified by the differences in lithofacies of Well A and lithology of Well B. Under SB3 interface, calcareous mudstone of S-3 was in Well A and calcareous mudstone of CM-1 was in Well B (Figs. 2, 5c and 5h). At interface of SB3, argillaceous mudstone of S-1 was deposited in Well A and siliceous mudstone of S-3 was deposited in Well B (Figs. 2, 5c and 5h). Sequence Boundary #4: SB4 was identified by the differences in lithology and lithofacies (Figs. 2 and 5). Under SB4 interface, calcareous mudstone of M-1 was in Well A and mudstone of M-2 was in Well B (Figs. 2, 5d and 5i). At interface of SB4, argillaceous limestone of C-1 was in Well A and argillaceous limestone of C-3 was in Well B (Figs. 2, 5d and 5i). Sequence Boundary #5: SB5 was identified due to the lithological differences between the Liujiang Formation and the underlying Luofu Formation (Figs. 2 and 5). Under SB5 interface, siliceous mudstone of S was deposited in Well A and calcareous mudstone of M-2 was deposited in Well B (Figs. 2, 5e and 5j). At interface of SB5, limestone was deposited in the Liujiang Formation of the A and B wells (Figs. 2, 5e and 5j).

According to the SBs, the sedimentary environment indicators and organic matter accumulation factors will be discussed in the four stages (Fig. 6a–b). Stage 1 is between SB1 and SB2. It is mainly composed of

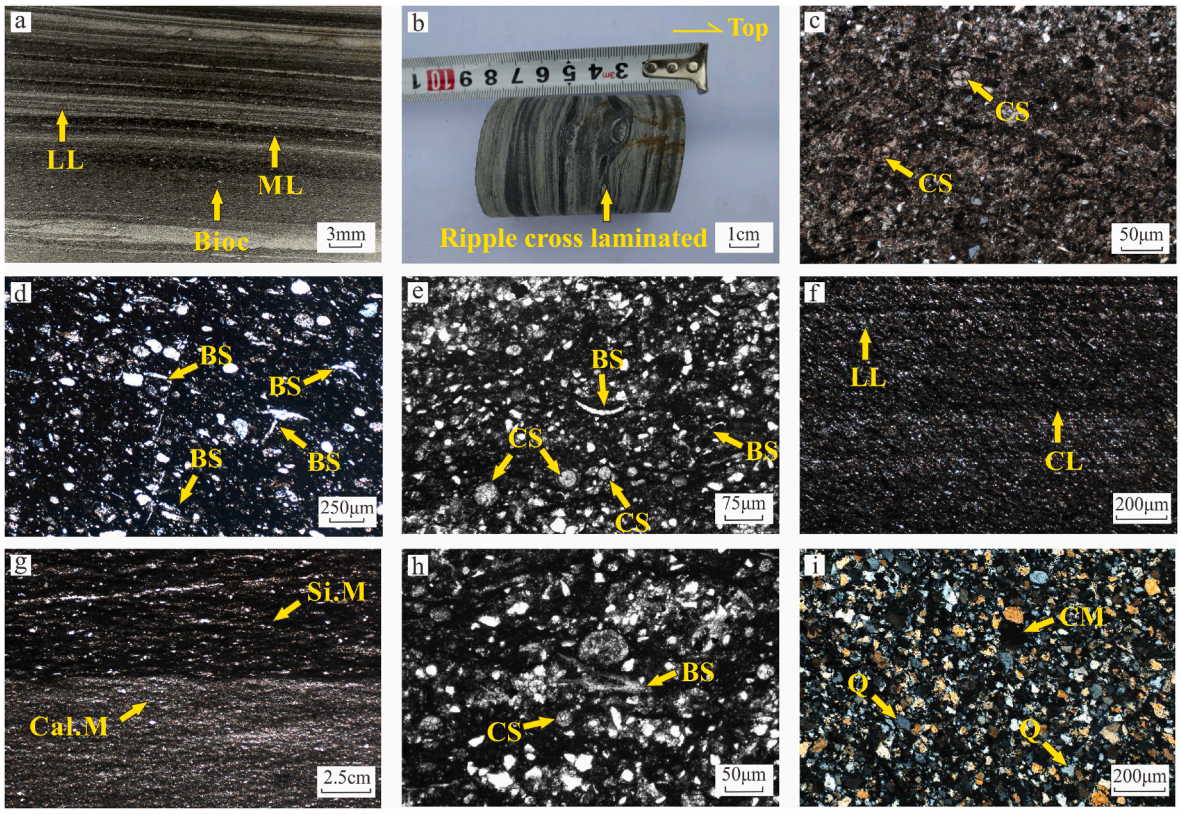

Fig. 4. The thin section optical microscopy images of representative mineral, and rock from the Luofu Formation. (a) The parallel bedding of Well A (1178.40 m); (b) The ripple cross laminated in the calcareous mudstone of Well B (489.10 m); (c) The calcite spherules in the calcareous mudstone of Well A (1268.00 m); (d) A large number of broken shells in the calcareous mudstone of Well A (1203.75 m); (e) The calcite spherules and broken shells in the calcareous mudstone of Well B (431.25 m); (f) The parallel bedding of Well A (1141.10 m); (g) The boundary between calcareous mudstone and siliceous mudstone in Well B (408.65 m); (h) The calcite spherules and broken shells in the calcareous mudstone of Well A (1020.20 m); (i) A large number of terrigenous detrital particles with low structural maturities (Well A, 999.3 m); Note that the photomicrographs (c–h) are captured under mono-polarized light and the photomicrograph (i) is captured under cross-polarized light; Bioc = bioclast; LL = limestone laminae; CS = calcite spherule; BS = broken shell; CL = calcareous laminae; Si. M = siliceous mudstone; Cal. M = calcareous mudstone; CM = clay mineral; Q = quartz.

calcareous mudstone of S-3 in Well A and mudstone of M-2 in Well B. Stage 2 (between SB2 and SB3) is mainly composed of calcareous mudstone of S-3 in Well A and calcareous mudstone of M-2 in Well B. Stage 3 (between SB3 and SB4) is composed of calcareous mudstone of M-2 and M-1 in Well A. In Well B, calcareous mudstone of S-3 and mudstone of M-2 are the upper and lower parts of stage 3, respectively. Stage 4 (between SB4 and SB5) is mainly composed of argillaceous limestone of C-1 and limestone of C-1 in Well A and argillaceous limestone of C-3 in Well B.

4.4. Total organic carbon content and organic matter petrography

The TOC content of Well B is considerably higher than that of Well A (Fig. 5). The TOC values of samples from the Luofu Formation in Well A range from 0.38% to 1.50%, with an average of 0.80%. 32 samples taken from Well B in the same formation have TOC values between 0.43% and 3.02%, with a higher average value of 1.52%. There is a noticeable difference in the TOC content of both wells for each sequence (Table 2). For stage 1 and stage 2 of Well A, the TOC content is relatively low, averaging 0.66% and 0.71%, respectively. While the relative low TOC content of Well B is in stage 4 (average 0.63%). In both wells, the highest TOC content (mean 1.17% of Well A; mean 2.16% of Well B) is in stage 3.

The whole-rock sections suggest that organic matter in the Luofu Formation is made up of sapropelinite (Fig. 7a), exinite (Fig. 7b) and vitrinite (Fig. 7c). Sapropelinite is a component formed by algae after sapropelic action (International Committee for Coal and Organic Petrology, 1998). At the overmature stage, residual algal forms should be visible, with no fluorescence display. Significantly, the high maturity of our samples makes it difficult to distinguish other oil-rich organic components like sapropelinite in the whole-rock section (Fig. 7a). Exinite is generally the reproductive organ of higher plants (International Committee for Coal and Organic Petrology, 1998). It appears grayish white under white reflected light in the Luofu Formation (Fig. 7b). Vitrinite is derived from botanical tissues, and lignin and/or carbohydrates are the main components of botanical tissues (International Committee for Coal and Organic Petrology, 1998;.Liu et al., 2023a) Under oil-immersed reflected light, over mature vitrinite can appear gray with high relief (Fig. 7c).

In order to reduce the effect of over-maturation on the identification of organic macerals, the kerogens extracted from the Luofu Formation mudstone were examined. In stage 1 and stage 2, a large amount of sapropelinite was developed in the A and B wells (Fig. 7f), and most of the kerogen belonged to type I (Appendix 1). In stage 3, sapropelinite was the main component of the macerals of kerogen (Fig. 7d–e), suggesting a main contribution of marine algae (Wu et al., 2022). All the kerogen of stage 3 belonged to type I (Appendix 1). Moving upwards to stage 4, the content of exinite and vitrinite increased, leading to the transition of the kerogen in Well A to type II_I, while type II_1 appeared in Well B (Appendix 1).

The organic matter adsorbed on the clay mineral surfaces or resides between the clay mineral interlayers forms a large number of organo-mineral complexes in stage 3 of Well A (Fig. 8a–c) and stage 2 of Well B (Fig. 8d–f). The complexes were directional and mostly lenticular in

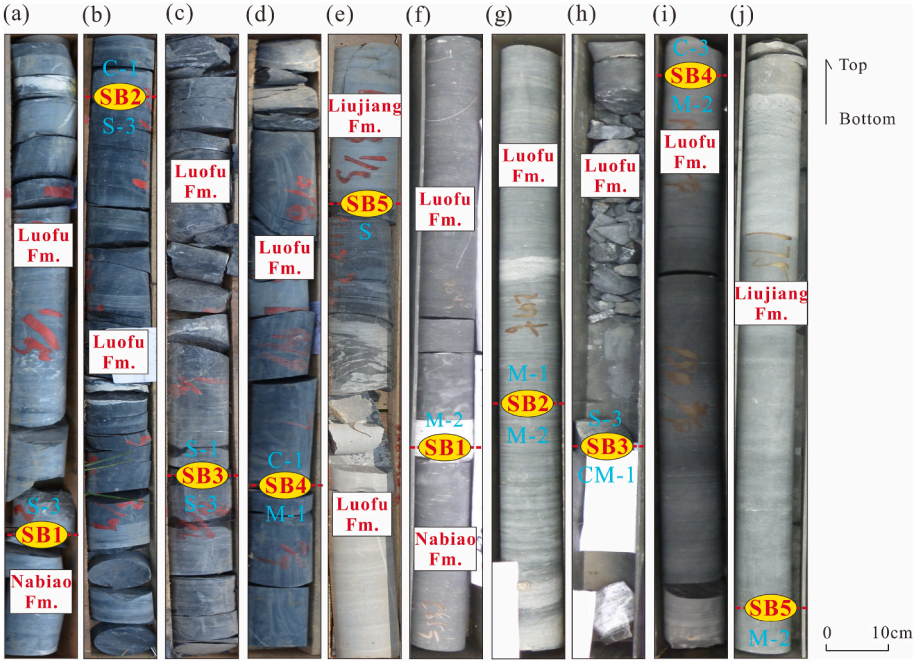

Fig. 5. Sequence boundaries, petrology and lithofacies characteristics. SB: Sequence boundary. (a) Sequence boundary 1 (Well A, 1420.10 m); (b) Sequence boundary 2 (Well A, 1309.00 m); (c) Sequence boundary 3 (Well A, 1154.50 m); (d) Sequence boundary 4 (Well A, 1082.00 m); (e) Sequence boundary 5 (Well A, 989.25 m); (f) Sequence boundary 1 (Well B, 624.00 m); (g) Sequence boundary 2 (Well B, 510.00 m); (h) Sequence boundary 3 (Well B, 408.50 m); (j) Sequence boundary 4 (Well B, 375.95 m); (i) Sequence boundary 5 (Well B, 320.00 m). The sequence divisions refer to Fig. 2.

shape (Fig. 8a–d). Organic matter was developed in interlayered arrangement with clay minerals typically exhibiting elongated shape (Fig. 8a–e). In other complexes, organic matter was locally enriched in large amounts, with discontinuous development of clay minerals (Fig. 8f). The complexes of the Luofu Formation exhibited coexistence of clay minerals and goethite (Fig. 8c, f).

4.5. Petrographic features of pyrite

SEM and polished section observations show that pyrite framboids are rare in stage 1, almost absent in stage 2, and abundant in stage 3 (Fig. 9). Various pyrite morphologies are observed in the Luofu Formation, including normal framboids (Fig. 9a–h), overgrown framboids (Fig. 9i), euhedral crystals (Fig. 9j and k), and clustered crystals (Fig. 9l). The normal framboids (Fig. 9a–h) occur in stage 1 and stage 2. In stage 1, the overgrown framboids (Fig. 9i) and clustered crystals (Fig. 9l) are observed. Within stage 2 and stage 4 of the Luofu Formation, the predominant form of pyrite is euhedral crystals (as depicted in Fig. 9j and k). These euhedral crystals exhibit a uniform internal structure.

The pyrite framboids found in Well A samples from stage 1 exhibit a predominant diameter exceeding 8 μm (with a mean range of 8.30–11.30 μm), (Fig. 10a and b). The pyrite framboids in Well B samples from the same section range from 1.70 to 13.30 μm in diameter (mean range of 6.10–7.98 μm) (Fig. 10c and d). In stage 3, framboidal pyrites are observed in Well A with a general size range of 4–8 μm (mean range of 5.99–6.12 μm) (Fig. 10e and f). In contrast, Well B contains a substantial abundance of framboidal pyrites measured approximately 2–6 μm (with a mean range of 4.20–4.80 μm) (Fig. 10g and h).

4.6. Elemental geochemistry

4.6.1. Major elements

The main major elements, expressed as oxides, are listed in Table 2. For samples from Well A, over 80% of the total oxides are composed of SiO_2 (average 55.69 wt%), Al_2O_3 (average 13.66 wt%), CaO (average 8.33 wt%) and Fe_2O_3 (average 3.84 wt%). For samples from Well B, over 70% of the total oxides are composed of SiO_2 (average 50.89 wt%), Al_2O_3 (average 12.85 wt%), CaO (average 6.74 wt%) and Fe_2O_3 (average 4.27 wt%). The concentrations of TiO_2 remain generally below 1 wt% in all the analyzed samples. The relative concentrations of major elements exhibit noticeable vertical fluctuations in both wells. In Well A, the SiO_2 contents are relatively high in stage 1 (average 59.89 wt%) and stage 2 (average 56.95 wt%), accompanied by the appearance of relatively high concentrations of bio-silicon (Si_{bio}) in stage 1 (average 12.12 wt%) and stage 2 (average 11.41 wt%). In stage 3, the contents of CaO (average 20.23 wt%) and the values of DOP_T (average 0.76%) are significantly higher than those of other stages. In stage 4, although the contents of SiO_2 are generally over 50 wt% (average 54.34 wt%), the contents of Si_{bio} are very low (average 4.07 wt%). The concentrations of SiO_2 values of samples from stage 1 of Well B range from 31.85 wt% to 58.84 wt%, with an average of 44.58 wt%. In stage 2, the contents of SiO_2 range from 40.50 wt% to 65.64 wt%, with an average of 54.34 wt %. In stage 3, the contents of SiO_2 (average 62.83 wt%) and Si_{bio} (average 16.42 wt%) and the values of DOP_T (average 0.53%) are relatively high. In stage 4, the average contents of SiO_2 (average 46.31 wt%) and Si_{bio} (average 7.73 wt%) and the values of DOP_T (average 0.20%) are relatively low.

4.6.2. Trace elements

The primary trace elements along with their corresponding analysis indices are listed in Table 3. Notably, the Luofu Formation exhibits substantial variations in the degrees of enrichment for trace elements, as indicated in Table 3.

In stage 1, samples of Well A show relatively low values of V/Cr (average 1.94), V_{EF} (average 1.45) and Ba_{bio} (average 340.73 wt%). The relatively low values of V/Cr (average 1.79), V_{EF} (average 1.69) and Ba_{bio} (average 340.73 wt%) are also shown in stage 2. In stage 3, the values of V/Cr (average 2.47), V_{EF} (average 1.96) and Ba_{bio} (average 387.61 wt%) are significantly higher than those of other stages. In stage 4, the average values of V/Cr (average 1.30), V/(V + Ni) (average 0.62), V_{EF} (average 1.01), and Ba_{bio} (average 104.97 wt%) remain generally below the average values of all the Luofu Formation samples in Well A.

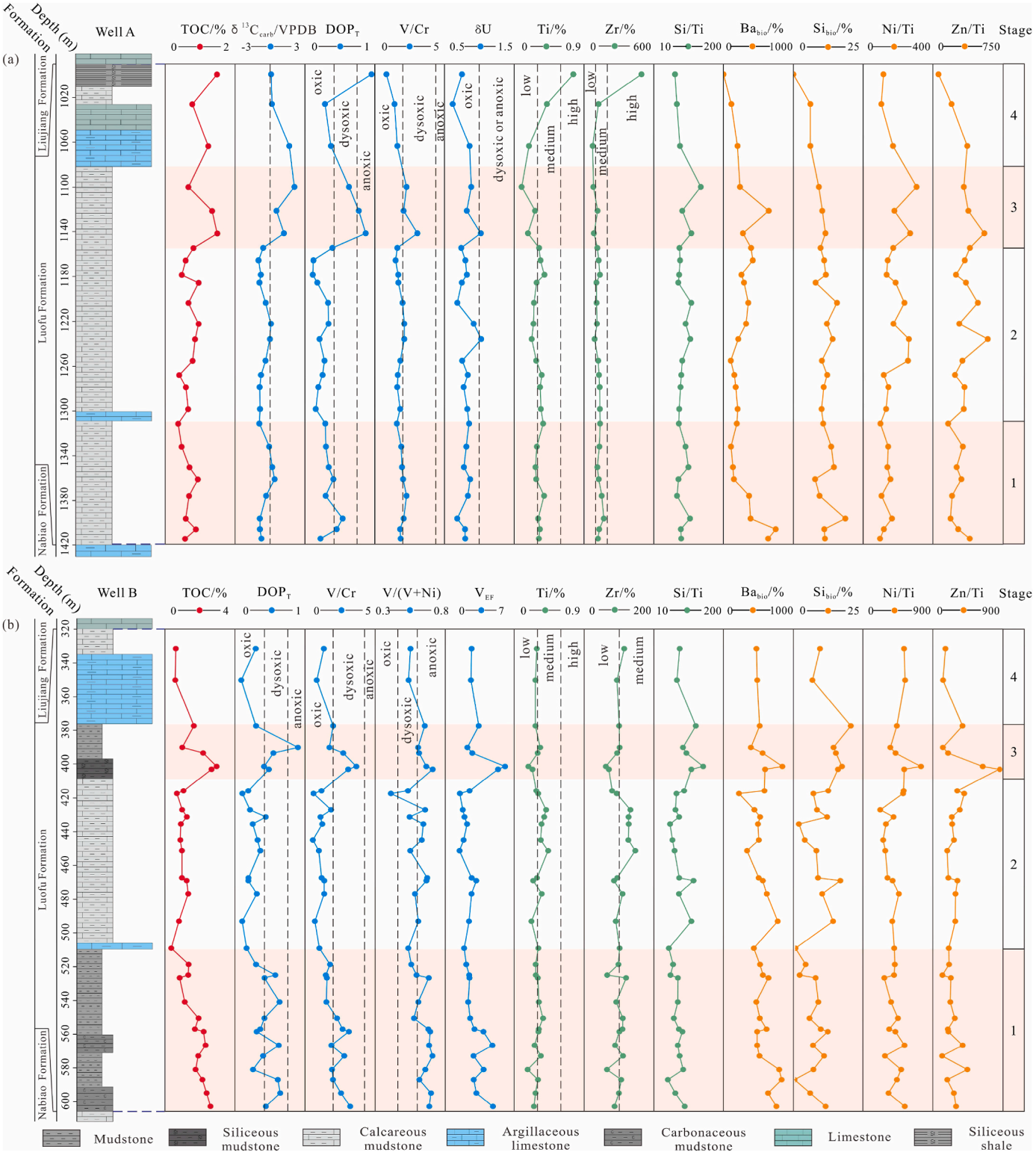

Fig. 6. Vertical variations of multiple geochemical proxies from the Luofu Formation of Well A (a) and Well B (b). Representative concentrations of Ba and Si from PAAS vs. Ti (Ba/Ti = 0.0065; Si/Ti = 2.93) and the indication meaning of all analysis indexes are indicated by the black vertical dashed lines (threshold values in Section 5).

In stage 1, samples of Well B show relatively high ratios of V/Cr (avg. 2.13), V/(V + Ni) (avg. 0.64), V_{EF} (avg. 3.03), and Ba_{bio} (avg. 577.01%). The low values of V/Cr (avg. 1.10), V/(V + Ni) (avg. 0.59), V_{EF} (avg. 2.16), and Ba_{bio} (avg. 263.53%) are in stage 2. In stage 3, the high values of V/Cr (avg. 2.64), V/(V + Ni) (avg. 0.65), V_{EF} (avg. 3.90), and DOP_T (avg. 0.53) are observed in Well B. For samples of stage 4, the average values of V/Cr, V/(V + Ni), V_{EF} and Ba_{bio} are 1.09, 0.55, 2.61 and 463.95 wt%, respectively.

4.7. Inorganic carbon isotope

Only where Mn/Sr value is less than 10, the $\delta^{13}C_{carb}$ likely records

Table 2
Geochemical indices, analysis indices, and partial major oxide contents of the Luofu Formation samples from Well A and Well B in the Youjiang Basin.

Stage	4	4	4	3	3	3	2	2	2	2	2	2	2	2
Depth/m	999.30	1026.04	1063.60	1100.10	1121.60	1141.40	1154.40	1165.50	1178.40	1185.60	1203.60	1222.20	1235.90	1255.30
Well-Sample ID	A-1	A-2	A-3	A-4	A-5	A-6	A-7	A-8	A-9	A-10	A-11	A-12	A-13	A-14
TOC/%	1.49	0.78	1.24	0.67	1.35	1.50	0.82	0.59	0.48	0.96	0.67	0.96	0.86	0.79
S/%	2.67	0.91	0.90	0.68	3.48	2.19	1.83	0.56	0.44	0.68	1.23	1.06	0.77	1.27
SiO_2/%	72.17	57.61	33.25	29.69	50.60	43.42	54.83	59.54	66.18	47.66	60.40	52.03	53.91	51.85
TiO_2/%	1.27	0.70	0.32	0.16	0.45	0.30	0.54	0.57	0.65	0.48	0.42	0.41	0.38	0.47
Al_2O_3/%	9.91	17.92	7.49	2.97	13.82	7.82	15.39	17.91	15.36	14.04	13.94	12.66	13.75	13.17
Fe_2O_3/%	3.48	3.97	3.00	1.33	5.61	3.13	5.77	5.74	4.87	4.80	4.62	3.90	4.55	5.64
MnO/%	0.04	0.04	0.04	0.03	0.04	0.04	0.06	0.04	0.05	0.25	0.06	0.05	0.07	0.20
CaO/%	1.53	3.55	23.46	34.11	7.35	19.22	5.05	2.51	1.97	12.68	5.84	11.50	9.46	8.54
K_2O/%	2.07	4.33	1.37	0.52	2.22	1.44	2.84	3.52	3.03	2.86	2.63	2.48	2.49	2.61
Si/%	33.68	26.88	15.52	13.85	23.61	20.26	25.59	27.79	30.88	22.24	28.19	24.28	25.16	24.20
Si_{bio}/%	0.00	6.10	6.10	9.15	10.35	11.50	9.75	11.03	11.64	7.97	15.64	12.03	14.05	10.23
Ti/%	0.76	0.42	0.19	0.10	0.27	0.18	0.32	0.34	0.39	0.29	0.25	0.25	0.23	0.28
Al/%	5.24	9.49	3.96	1.57	7.32	4.14	8.15	9.48	8.13	7.43	7.38	6.70	7.28	6.97
Fe/%	2.44	2.78	2.10	0.93	3.92	2.19	4.04	4.02	3.41	3.36	3.23	2.73	3.19	3.95
Mn/%	0.03	0.03	0.03	0.02	0.03	0.03	0.04	0.03	0.04	0.20	0.05	0.04	0.05	0.15
Si/Ti	44.32	64.00	81.68	138.50	87.44	112.56	79.97	81.74	79.18	76.69	112.76	97.12	109.39	86.43
$\delta^{13}C_{carb}$//VPDB	0.09	0.16	1.65	2.10	0.55	1.19	−0.60	−0.99	−0.79	−0.91	−0.37	0.08	−0.01	−0.40
DOP_T	0.95	0.29	0.37	0.63	0.77	0.87	0.39	0.12	0.11	0.18	0.33	0.34	0.21	0.28
Stage	2	2	2	1	1	1	1	1	1	1	1	4	4	3
Depth/m	1267.90	1279.10	1298.40	1311.40	1332.20	1350.40	1361.15	1376.20	1396.40	1406.00	1414.60	331.50	350.10	377.30
Well-Sample ID	A-15	A-16	A-17	A-18	A-19	A-20	A-21	A-22	A-23	A-24	A-25	B-1	B-2	B-3
TOC/%	0.41	0.60	0.66	0.38	0.48	0.70	0.94	0.69	0.59	0.89	0.57	0.69	0.56	1.72
S/%	0.86	0.77	0.58	0.76	1.00	0.99	1.42	1.01	1.43	1.31	0.53	0.82	0.13	0.54
SiO_2/%	63.51	58.47	58.03	62.36	59.93	60.21	46.65	60.78	72.50	58.84	57.85	50.15	42.47	71.86
TiO_2/%	0.59	0.56	0.57	0.62	0.49	0.46	0.47	0.64	0.51	0.55	0.53	0.49	0.46	0.46
Al_2O_3/%	16.96	17.34	17.94	17.76	13.26	12.46	12.38	19.20	11.30	14.00	12.72	14.05	12.13	16.65
Fe_2O_3/%	4.24	5.01	4.68	3.22	4.13	3.63	4.33	4.23	3.29	3.58	2.94	3.43	1.77	2.23
MnO/%	0.03	0.06	0.05	0.03	0.03	0.04	0.07	0.02	0.04	0.03	0.03	0.03	0.02	0.03
CaO/%	2.65	4.19	4.42	3.23	7.25	7.28	13.42	1.96	2.25	6.12	8.64	8.03	4.03	6.05
K_2O/%	3.54	3.50	3.78	3.79	2.60	2.39	2.36	3.89	2.35	3.02	2.76	3.38	3.14	3.25
Si/%	29.64	27.28	27.08	29.10	27.97	28.10	21.77	28.37	33.83	27.46	26.99	23.43	19.84	33.58
Si_{bio}/%	12.14	10.86	10.12	10.69	13.55	14.54	7.80	9.36	18.62	11.09	11.31	9.08	6.37	20.08
Ti/%	0.35	0.33	0.34	0.37	0.29	0.27	0.28	0.39	0.31	0.33	0.32	0.29	0.27	0.27
Al/%	8.98	9.18	9.50	9.40	7.02	6.60	6.56	10.16	5.98	7.41	6.73	7.44	6.42	8.81
Fe/%	2.97	3.51	3.27	2.26	2.89	2.54	3.03	2.96	2.30	2.51	2.06	2.40	1.24	1.56
Mn/%	0.02	0.05	0.04	0.02	0.02	0.03	0.05	0.01	0.03	0.02	0.02	0.03	0.02	0.02
Si/Ti	84.69	82.67	79.65	78.65	96.45	104.07	77.75	72.74	109.13	83.21	84.34	80.79	73.48	124.37
$\delta^{13}C_{carb}$//VPDB	−0.78	−0.89	−0.86	−0.92	−0.08	0.19	0.39	−0.34	−0.88	−0.87	−0.74	–	–	–
DOP_T	0.25	0.19	0.15	0.29	0.30	0.34	0.41	0.30	0.54	0.45	0.22	0.30	0.09	0.30
Stage	3	3	3	3	2	2	2	2	2	2	2	2	2	2
Depth/m	390.10	393.30	401.30	402.90	415.70	417.30	426.90	431.10	435.30	444.90	451.30	467.30	468.90	476.90
Well-Sample ID	B-4	B-5	B-6	B-7	B-8	B-9	B-10	B-11	B-12	B-13	B-14	B-15	B-16	B-17
TOC/%	1.06	2.25	3.02	2.73	1.13	0.75	1.05	1.32	0.98	0.95	1.04	1.04	1.31	1.40
S/%	2.34	1.89	0.61	0.91	0.99	0.91	0.69	2.07	1.31	1.31	1.53	0.90	0.80	1.60
SiO_2/%	65.23	63.49	55.55	58.03	55.84	47.04	60.58	65.64	40.50	44.07	62.88	48.94	60.81	58.56
TiO_2/%	0.56	0.50	0.31	0.39	0.48	0.52	0.69	0.65	0.59	0.57	0.73	0.49	0.41	0.59
Al_2O_3/%	15.25	16.71	6.67	9.92	17.37	17.67	14.25	18.31	10.51	10.67	14.34	10.82	15.96	19.32
Fe_2O_3/%	3.24	4.29	1.83	2.34	6.43	10.54	3.97	5.87	6.37	5.03	5.26	5.74	5.17	6.38
MnO/%	0.03	0.04	0.03	0.02	0.05	0.07	0.03	0.03	0.05	0.03	0.04	0.04	0.04	0.03
CaO/%	5.62	7.00	14.32	5.38	5.11	13.92	2.98	3.07	5.07	4.91	5.81	5.89	8.36	5.56

(*continued on next page*)

Table 2 (*continued*)

Stage	3	3	3	3	2	2	2	2	2	2	2	2	2	2
K_2O/%	3.44	3.34	1.55	2.61	3.45	1.77	3.38	3.30	3.49	4.61	2.79	3.25	3.08	3.69
Si/%	30.48	29.67	25.96	27.12	26.09	21.98	28.31	30.67	18.93	20.59	29.39	22.87	28.42	27.36
Si_{bio}/%	13.93	14.75	16.93	15.50	12.04	6.74	8.01	11.62	1.55	3.64	7.81	8.39	16.34	9.87
Ti/%	0.34	0.30	0.18	0.24	0.28	0.31	0.41	0.39	0.35	0.34	0.44	0.29	0.24	0.35
Al/%	8.07	8.84	3.53	5.25	9.19	9.35	7.54	9.69	5.56	5.64	7.59	5.73	8.44	10.22
Fe/%	2.27	3.00	1.28	1.64	4.50	7.38	2.78	4.11	4.46	3.52	3.68	4.02	3.62	4.46
Mn/%	0.02	0.03	0.02	0.02	0.04	0.06	0.02	0.03	0.04	0.02	0.03	0.03	0.03	0.03
Si/Ti	89.65	98.90	144.22	113.00	93.18	70.90	69.05	78.64	54.09	60.56	66.80	78.86	118.42	78.17
$\delta^{13}C_{carb}$//VPDB	–	–	–	–	–	–	–	–	–	–	–	–	–	–
DOP_T	0.90	0.55	0.41	0.48	0.19	0.11	0.22	0.44	0.26	0.32	0.36	0.19	0.19	0.31
Stage	2	2	1	1	1	1	1	1	1	1	1	1	1	1
Depth/m	493.10	509.20	518.70	525.10	526.70	541.10	550.70	557.10	558.70	566.70	573.10	581.10	587.10	595.10	603.10
Well-Sample ID	B-18	B-19	B-20	B-21	B-22	B-23	B-24	B-25	B-26	B-27	B-28	B-29	B-30	B-31	B-32
TOC/%	0.87	0.43	1.42	1.40	0.91	1.20	1.99	1.78	2.28	2.39	1.97	1.82	2.21	2.45	2.67
S/%	0.37	0.62	1.34	1.20	1.08	2.45	1.72	1.08	0.72	2.14	0.94	0.75	1.24	1.93	1.06
SiO_2/%	52.91	33.62	37.71	33.35	48.22	51.69	50.72	53.53	58.40	41.85	58.84	32.75	31.85	41.00	50.55
TiO_2/%	0.37	0.52	0.46	0.47	0.51	0.53	0.62	0.53	0.52	0.44	0.57	0.29	0.51	0.46	0.42
Al_2O_3/%	15.19	12.21	8.07	9.83	11.80	13.99	14.34	13.93	13.20	11.66	15.29	5.88	9.01	8.58	7.46
Fe_2O_3/%	4.40	4.62	5.54	2.59	3.19	4.79	5.10	3.72	2.88	4.26	2.92	3.60	2.52	3.72	2.99
MnO/%	0.03	0.04	0.05	0.04	0.03	0.02	0.03	0.03	0.03	0.05	0.02	0.03	0.02	0.02	0.02
CaO/%	5.33	6.57	9.93	21.70	5.46	4.37	6.56	4.73	7.51	16.38	2.55	3.69	1.09	6.80	1.75
K_2O/%	3.79	3.02	2.40	2.37	3.34	3.24	3.44	3.40	3.02	2.53	3.44	2.78	3.58	3.14	3.18
Si/%	24.72	15.71	17.62	15.59	22.53	24.16	23.70	25.01	27.29	19.56	27.50	15.31	14.88	19.16	23.62
Si_{bio}/%	13.76	0.35	3.96	1.83	7.52	8.47	5.35	9.35	11.88	6.59	10.53	6.74	0.00	5.59	11.09
Ti/%	0.22	0.31	0.28	0.28	0.30	0.32	0.37	0.32	0.31	0.26	0.34	0.17	0.31	0.28	0.25
Al/%	8.04	6.46	4.27	5.20	6.24	7.40	7.58	7.37	6.99	6.17	8.09	3.11	4.77	4.54	3.94
Fe/%	3.08	3.23	3.88	1.82	2.23	3.35	3.57	2.60	2.02	2.98	2.04	2.52	1.77	2.60	2.10
Mn/%	0.02	0.03	0.04	0.03	0.02	0.02	0.03	0.02	0.02	0.04	0.02	0.02	0.01	0.02	0.02
Si/Ti	112.36	50.68	62.93	55.68	75.10	75.50	64.05	78.16	88.03	75.23	80.88	90.06	48.00	68.43	94.48
$\delta^{13}C_{carb}$/VPDB	–	–	–	–	–	–	–	–	–	–	–	–	–	–	–
DOP_T	0.10	0.17	0.30	0.58	0.42	0.64	0.42	0.36	0.31	0.62	0.40	0.26	0.61	0.65	0.44

Note: "-" means no data.

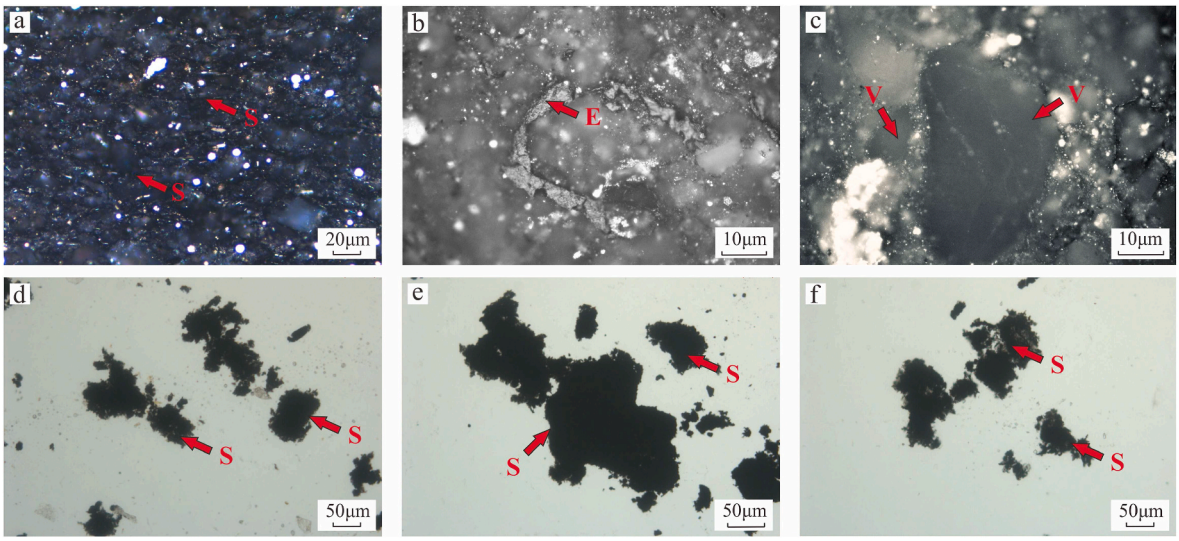

Fig. 7. Photomicrographs of transmission-fluorescence kerogen macerals and organic matter under reflected white light in oil immersion. (a) Sapropelinite of Well B (401.30 m); (b) Exinite of Well A (999.30 m); (c) Vitrinite of Well A (1063.60 m); (d) A large amount of sapropelinite in Well B (390.10 m); (e) A large amount of sapropelinite in Well B (401.30 m); (f) A large amount of sapropelinite in Well B (476.90 m); S = sapropelinite; E = exinite; V = vitrinite.

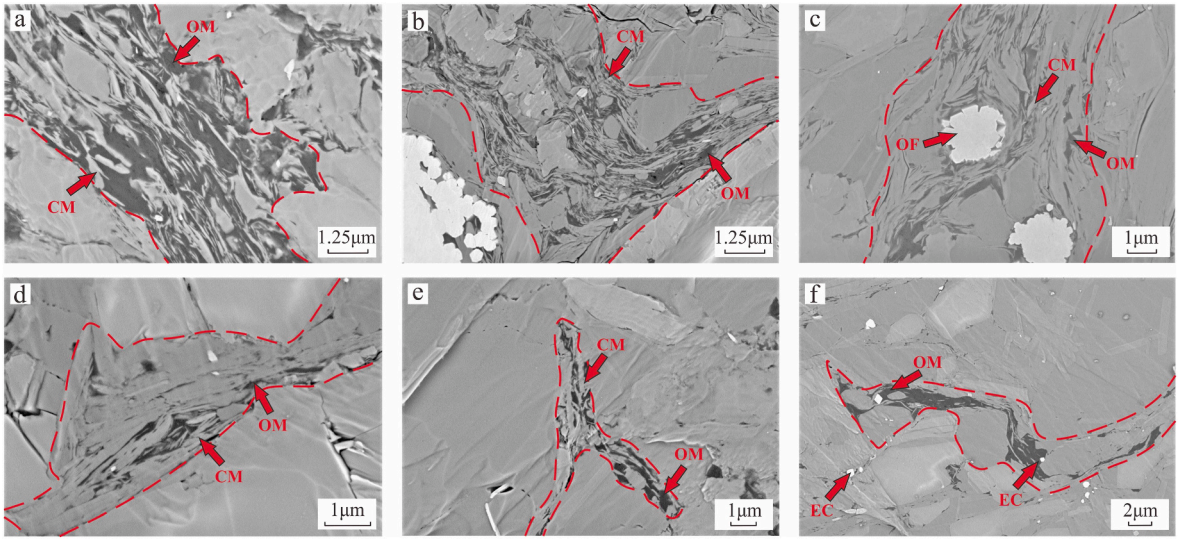

Fig. 8. SEM photos of organo-mineral complex in the Luofu Formation. (a) Organo-mineral complex of Well A (1279.10 m); (b) Organo-mineral complex of Well A (1121.60 m); (c) Organo-mineral complex of Well A (1141.40 m); (d) Organo-mineral complex of Well B (431.10 m); (e) Organo-mineral complex of Well B (451.30 m); (f) Organo-mineral complex of Well B (476.90 m); OM = organic matter; CM = clay mineral; EC = euhedral crystal; OF = overgrown framboid.

the carbonate primary carbon isotopic signature (Heath et al., 2021; Hu et al., 2021). Therefore, the values of Mn/Sr in the samples of the Luofu Formation were calculated, before using the $\delta^{13}C_{carb}$ values of Well A. The Mn/Sr values range from 0.16 to 3.15, with an average value of 0.97, all of which are below 10, with the majority falling below 3 (Table 2), suggesting that the $\delta^{13}C_{carb}$ values observed in the samples reflect the initial values of the original seawater.

The results of $\delta^{13}C_{carb}$ analysis of the samples are presented in Fig. 6a and Table 2. The $\delta^{13}C_{carb}$ values of stage 1 (−0.92 VPDB - 0.39 VPDB, mean −0.41 VPDB) and stage 2 (−0.99 VPDB - 0.08 VPDB, mean −0.59 VPDB) have a small fluctuation range. In contrast, stage 3 has an obvious positive deviation, and the values (0.55 VPDB - 2.10 VPDB, mean 1.28 VPDB) are much higher than before. Compared to stage 3, the values of stage 4 (0.09 VPDB - 1.65 VPDB, mean 0.68 VPDB) decrease significantly.

5. Discussion

5.1. Sequence stratigraphic framework

A sequence stratigraphic framework requires: (1) evidence showing chronostratigraphic equivalency of adjacent datasets using geological age or seismic data; and, (2) data across the basin to observe the basin-scale trends. Numerous previous studies have consistently demonstrated a correlation between higher GR values and the escalating clay content found in mudstone as the water column deepens during the deposition phase (Singh, 2008; Abouelresh and Slatt, 2012). In general, it has been accepted that such trends can be interpreted as T-R (transgressive/regressive) cycles that can be associated to systems tracts (LaGrange et al., 2020; Liu et al., 2023b). In this way, important sequence stratigraphic surfaces and trends can be inferred by vertical lithological distributions and the GR log (Luning et al., 2000). Similarly, within the Luofu Formation, 3–5 third-order sequences have been

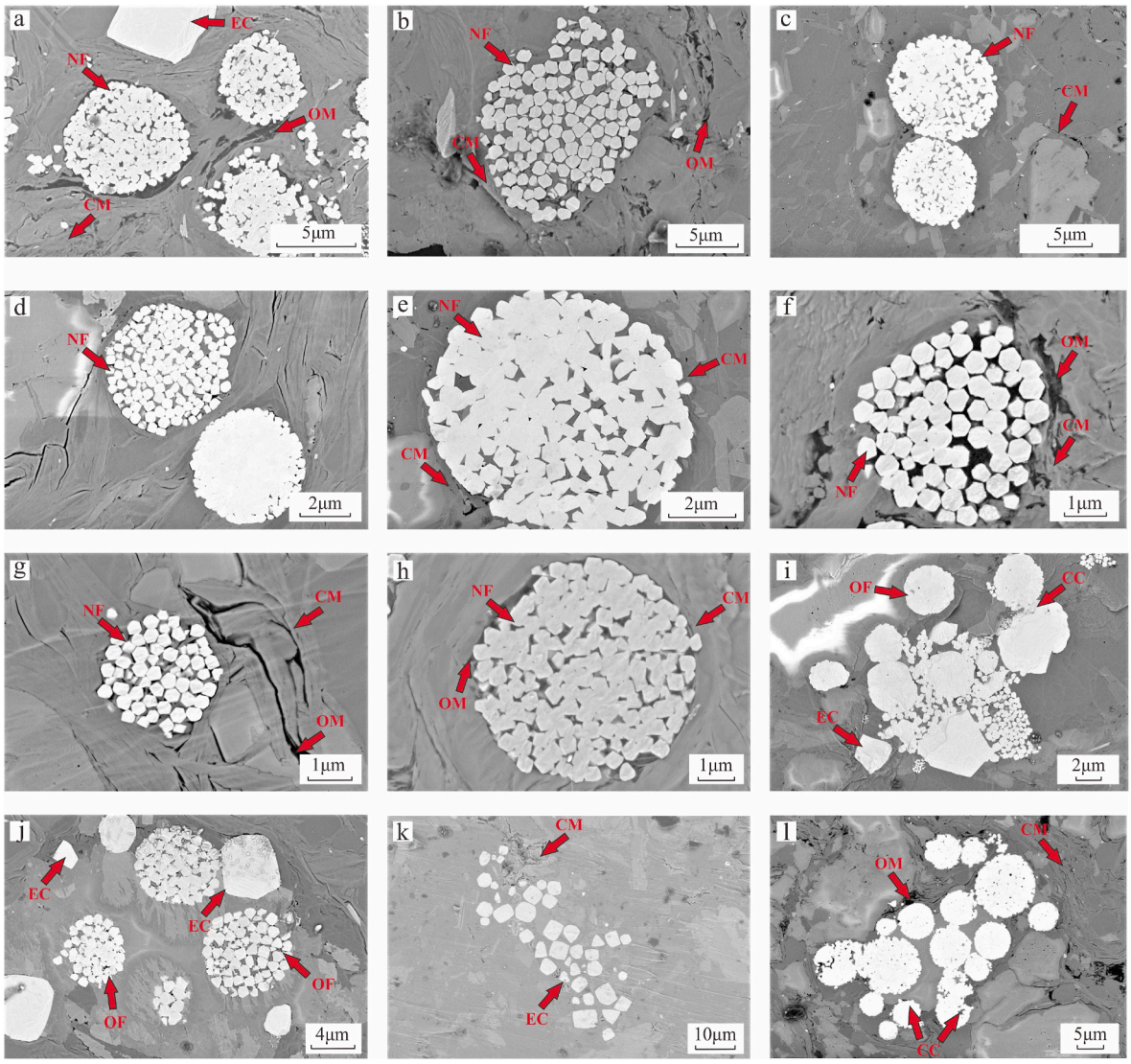

Fig. 9. SEM photos of pyrite in the Luofu Formation. (a) Normal framboid of Well A (1406.00 m); (b) Normal framboid of Well A (1361.15 m); (c) Normal framboid of Well B (595.10 m); (d) Normal framboid of Well B (573.10 m); (e) Normal framboid of Well A (1141.40 m); (f) Normal framboid of Well A (1121.60 m); (g) Normal framboid of Well B (401.30 m); (h) Normal framboid of Well B (393.30 m); (i) Overgrown framboid of Well A (1317.75 m); (j) Euhedral crystal of Well B (451.40 m); (k) Euhedral crystal of Well A (1203.75 m); (l) clustered crystal of Well B (512.12 m); OM = organic matter; CM = clay mineral; NF = normal framboid; OF = overgrown framboid; EC = euhedral crystal; CC = clustered crystal.

identified (Gong and Wu, 1997; Gong et al., 1994; Du et al., 1996, 1997, 2009). Geochemical and U–Pb dating evidences show that each sequence lasts about 1.25 Ma (Brett et al., 1990; Gradstein, 2020).

Based on the recognition of SBs, four third-order sequences of the Luofu Formation were interpreted. Each sequence of the Luofu Formation was composed of a lower transgressive systems tract (TST) and an upper regressive systems tract (RST) (Fig. 2). The boundary between a TST and an RST was identified as a maximum flooding surface (mfs) which corresponds to a relatively high GR value and mudstone content (Fig. 2).

5.2. Terrestrial detrital influx

The enrichment of organic matter is influenced by various factors, one of which is the influx of terrestrial detritus which can directly impact the enrichment of organic matter by diluting its concentration (Algeo and Maynard, 2004; Hou et al., 2022), or it can act as a sorbent for organic matter to facilitate its accumulation (Wang et al., 2019) and rate of settling (Playter et al., 2017). The mechanisms by which clay minerals affect organic matter accumulation can vary depending on the sedimentation rate, water column redox conditions, organic matter source, clay mineral surface area (Kennedy and Wagner, 2011), and other factors.

Al primarily originates from aluminosilicate clay minerals, whereas Ti is predominantly hosted in Ti-bearing heavy minerals (Jarvis et al., 2001; Pan et al., 2021). Al, Ti, Th, and Zr are commonly used as indicators of terrestrial detrital flux. Correlation diagrams reveal strong positive relationships between Ti and Th/Zr in both wells (Fig. 11a–b). The correlation between Al and Th or Zr is weak (Fig. 11c–d). Anomalies observed in the Al content may be ascribed to the presence of authigenic clay minerals (Wang et al., 2020; Wu et al., 2021; Zhao et al., 2022). Therefore, Si/Ti ratio is more suitable to trace the role of terrestrial detritus input in this study (Tribovillard et al., 1994; Rimmer, 2004).

The Yangtze platform has consistently imported terrigenous sediment from the northeast of the study area. As shown by the fact that the A and B wells generally have similar values of Ti Zr and Si/Ti (Fig. 6a–b), although the Nandan Rift Zone is geographically closer to the upper Yangtze uplift compared to the Baise Rift Zone (Fig. 1d), the presence of

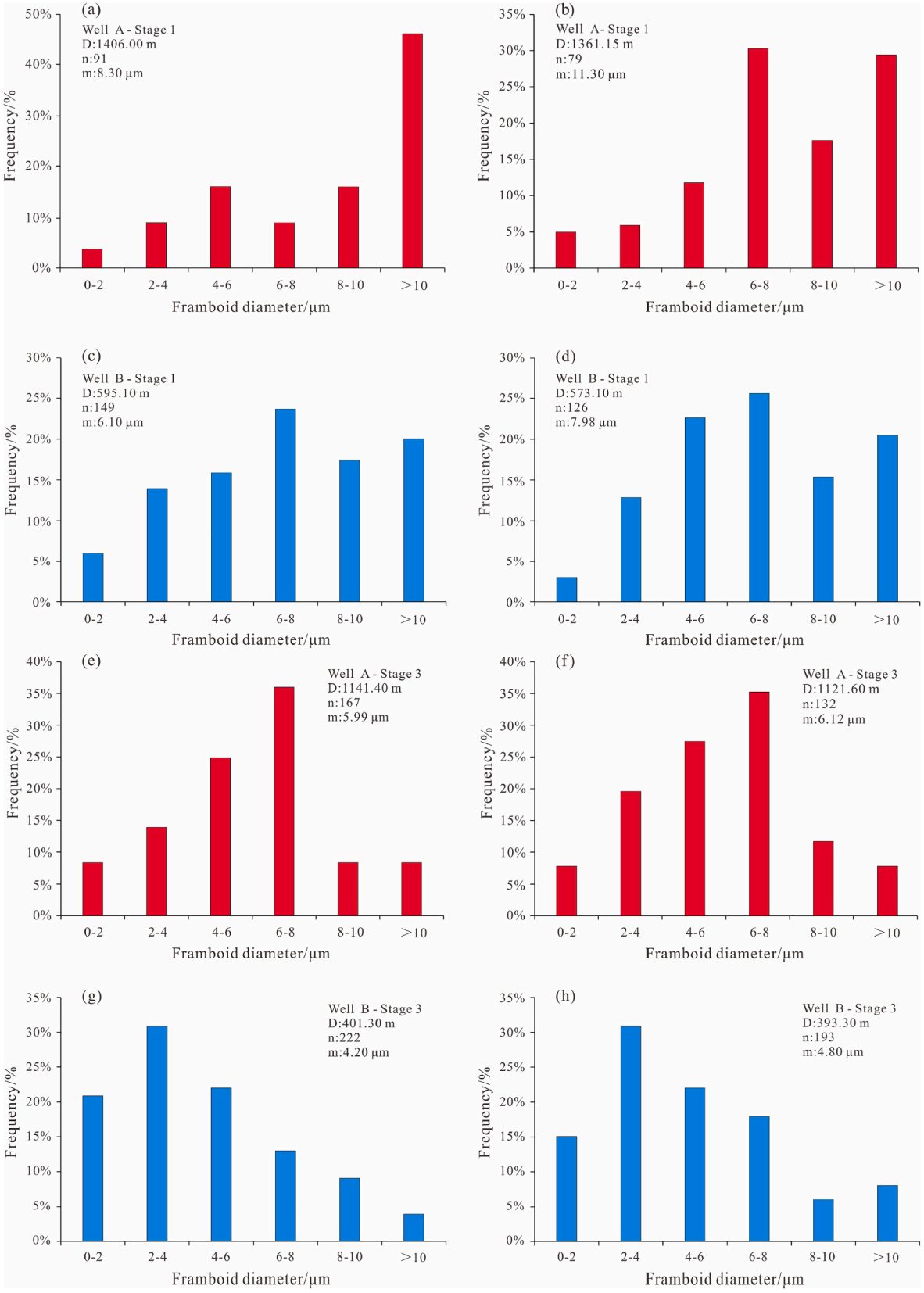

Fig. 10. Histograms showing the distribution of pyrite framboid diameters of stage 1 and stage 3 in the Luofu Formation, D = depth, n = number of measured framboids, mean = mean framboid diameter.

Table 3
Trace elements and analysis indices of the Luofu Formation samples from Well A and Well B in the Youjiang Basin.

Stage	4	4	4	3	3	3	2	2	2	2	2	2	2	2
Depth/m	999.30	1026.04	1063.60	1100.10	1121.60	1141.40	1154.40	1165.50	1178.40	1185.60	1203.60	1222.20	1235.90	1255.30
Well-Sample ID	A-1	A-2	A-3	A-4	A-5	A-6	A-7	A-8	A-9	A-10	A-11	A-12	A-13	A-14
V/ppm	69.85	130.90	67.96	37.34	122.77	110.73	146.35	144.16	125.46	129.73	104.37	99.00	111.32	114.28
Cr/ppm	83.08	92.27	41.79	16.37	59.30	36.19	90.10	96.21	74.29	76.44	52.28	46.71	52.51	62.14
U/ppm	5.01	3.28	1.76	9.26	10.75	13.25	6.59	4.76	4.21	2.97	3.29	2.29	3.09	2.98
Mo/ppm	0.77	0.45	0.59	6.39	9.56	13.20	2.20	2.44	1.56	1.39	1.01	0.89	0.99	1.01
Ni/ppm	88.47	43.90	32.66	29.24	48.18	47.90	55.44	47.87	52.51	53.89	60.27	43.17	59.05	72.85
Zn/ppm	45.52	84.52	70.55	31.74	102.48	98.26	127.75	116.31	96.92	102.77	123.17	70.51	132.76	89.85
Rb/ppm	114.46	252.77	85.80	31.89	131.52	84.30	172.00	207.05	174.05	167.51	144.22	132.00	140.83	148.38
Sr/ppm	104.06	238.28	928.05	1245.06	572.19	961.29	321.78	267.24	251.08	634.22	399.80	780.16	662.50	530.76
Zr/ppm	494.69	124.89	74.91	80.44	116.98	85.28	114.85	126.12	137.24	106.81	108.52	111.93	91.63	122.60
Nb/ppm	29.54	15.96	7.50	3.83	9.68	6.58	11.66	11.69	13.77	10.12	8.41	8.30	7.91	10.24
Ba/ppm	327.05	574.03	410.42	340.27	942.21	473.09	747.43	791.31	683.95	610.71	634.36	596.05	458.42	415.11
Th/ppm	25.04	22.02	6.98	4.35	11.13	6.74	13.23	11.82	12.09	12.21	11.34	8.09	5.95	13.77
V/Cr	0.84	1.42	1.63	2.28	2.07	3.06	1.62	1.50	1.69	1.70	2.00	2.12	2.12	1.84
V/(V + Ni)	0.44	0.75	0.68	0.56	0.72	0.70	0.73	0.75	0.70	0.71	0.63	0.70	0.65	0.61
U_{EF}	0.83	0.99	1.17	11.71	5.04	9.31	2.60	1.77	1.37	1.30	1.67	1.16	1.70	1.35
Mo_{EF}	0.18	0.19	0.56	11.50	6.37	13.20	1.24	1.29	0.72	0.86	0.73	0.64	0.77	0.65
V_{EF}	0.37	1.24	1.42	1.57	1.83	2.49	1.82	1.70	1.29	1.79	1.64	1.59	1.98	1.61
Mn/Sr	2.88	1.26	0.32	0.16	0.52	0.31	1.24	1.12	1.59	3.15	1.25	0.51	0.75	2.83
Ba_{bio}/%	0.00	113.24	201.68	235.90	648.14	278.79	396.25	419.79	257.29	294.33	356.04	324.30	212.27	105.29

Stage	2	2	2	1	1	1	1	1	1	1	1	4	4	3
Depth/m	1267.90	1279.10	1298.40	1311.40	1332.20	1350.40	1361.15	1376.20	1396.40	1406.00	1414.60	331.50	350.10	377.30
Well-Sample ID	A-15	A-16	A-17	A-18	A-19	A-20	A-21	A-22	A-23	A-24	A-25	B-1	B-2	B-3
V/ppm	141.32	148.62	153.30	149.21	109.29	99.12	98.18	148.78	101.39	120.18	107.52	191.86	175.22	228.98
Cr/ppm	85.37	92.12	83.90	93.96	57.36	50.65	48.24	65.21	48.79	65.91	57.84	143.08	210.43	114.19
U/ppm	3.71	3.91	3.85	3.54	2.75	2.29	2.38	3.62	2.36	2.93	2.72	0.30	1.03	32.03
Mo/ppm	0.56	0.44	0.66	0.40	0.89	0.50	0.55	0.48	0.73	0.72	0.84	0.40	0.89	21.25
Ni/ppm	41.94	48.22	45.32	37.04	41.98	38.24	44.35	40.61	51.05	39.47	30.82	155.59	149.88	121.18
Zn/ppm	84.33	113.01	114.26	61.34	94.10	70.28	86.72	79.64	58.48	90.34	126.16	42.67	31.86	100.11
Rb/ppm	200.69	202.49	213.30	215.19	148.99	130.17	124.57	204.13	123.87	164.75	146.44	180.13	72.54	83.31
Sr/ppm	403.20	478.10	521.05	508.49	672.63	652.08	894.42	421.47	241.98	462.97	506.30	233.26	167.94	142.81
Zr/ppm	129.10	135.12	136.87	138.43	132.92	115.49	126.67	152.57	170.84	130.91	120.45	114.26	93.43	99.65
Nb/ppm	12.72	11.96	12.63	13.47	10.77	10.22	10.12	13.28	11.73	12.94	11.93	8.33	8.65	7.52
Ba/ppm	543.21	539.18	579.20	599.28	427.61	436.25	459.36	788.50	726.39	1109.11	987.38	776.38	768.42	803.98
Th/ppm	11.34	13.83	12.12	14.29	12.02	10.77	9.33	15.15	13.64	13.30	12.30	9.70	8.94	10.35
V/Cr	1.66	1.61	1.83	1.59	1.91	1.96	2.04	2.28	2.08	1.82	1.86	1.34	0.83	2.01
V/(V + Ni)	0.77	0.76	0.77	0.80	0.72	0.72	0.69	0.79	0.67	0.75	0.78	0.55	0.54	0.65
U_{EF}	1.34	1.50	1.43	1.21	1.20	1.07	1.08	1.18	0.96	1.12	1.08	0.13	0.48	15.01
Mo_{EF}	0.29	0.24	0.35	0.19	0.55	0.34	0.36	0.22	0.43	0.39	0.47	0.25	0.59	14.17
V_{EF}	1.59	1.79	1.78	1.60	1.50	1.44	1.39	1.54	1.32	1.45	1.35	2.64	2.57	3.35
Mn/Sr	0.50	1.05	0.77	0.39	0.30	0.46	0.56	0.24	1.24	0.43	0.40	1.29	1.19	1.40
Ba_{bio}/%	155.28	174.88	203.09	191.00	107.94	135.62	149.54	367.09	389.00	746.12	639.49	458.17	469.73	504.65

Stage	3	3	3	3	2	2	2	2	2	2	2	2	2	2
Depth/m	390.10	393.30	401.30	402.90	415.70	417.30	426.90	431.10	435.30	444.90	451.30	467.30	468.90	476.90
Well-Sample ID	B-4	B-5	B-6	B-7	B-8	B-9	B-10	B-11	B-12	B-13	B-14	B-15	B-16	B-17
V/ppm	185.76	204.45	273.60	310.52	173.26	113.32	180.13	185.97	192.42	157.85	157.48	193.98	189.62	233.10
Cr/ppm	106.96	75.07	74.78	100.91	147.75	188.05	97.10	168.58	156.63	284.40	159.78	164.23	138.41	170.78
U/ppm	21.36	46.63	35.00	15.20	5.09	1.86	4.73	3.82	1.09	5.48	2.14	1.56	4.06	5.16
Mo/ppm	31.36	75.16	36.26	31.96	1.56	1.53	8.86	3.66	0.53	1.34	6.15	4.80	8.86	4.11
Ni/ppm	120.45	128.86	137.81	126.41	151.08	161.44	94.19	154.65	106.50	91.58	128.48	94.67	95.18	166.15
Zn/ppm	38.30	54.69	114.66	196.48	85.06	119.73	136.49	88.48	82.36	88.17	74.33	54.14	73.68	97.80

(*continued on next page*)

Table 3 (*continued*)

Stage	3	3	3	3	2	2	2	2	2	2	2	2	2	2
Rb/ppm	83.99	80.61	42.76	65.96	83.83	37.04	83.31	78.20	78.80	78.85	68.97	76.66	69.61	88.91
Sr/ppm	138.43	200.52	215.85	134.93	119.78	143.70	145.53	140.25	167.60	141.81	151.77	198.85	246.32	185.39
Zr/ppm	101.20	93.91	61.92	70.59	79.70	92.78	132.08	126.73	127.09	126.08	145.89	94.49	85.06	109.37
Nb/ppm	9.01	10.81	5.74	7.55	9.95	6.95	12.04	10.30	8.88	10.92	12.69	8.97	6.85	9.34
Ba/ppm	746.25	877.28	526.43	639.39	883.72	547.01	879.26	932.59	865.28	868.61	803.56	811.26	817.63	993.30
Th/ppm	10.91	7.84	9.63	8.49	8.59	10.33	12.83	11.39	10.61	9.80	14.70	9.60	10.27	12.67
V/Cr	1.74	2.72	3.66	3.08	1.17	0.60	1.86	1.10	1.23	0.56	0.99	1.18	1.37	1.36
V/(V + Ni)	0.61	0.61	0.67	0.71	0.53	0.41	0.66	0.55	0.64	0.63	0.55	0.67	0.67	0.58
U_{EF}	7.95	19.66	24.59	8.01	2.30	0.76	1.46	1.24	0.39	2.04	0.62	0.68	2.14	1.86
Mo_{EF}	16.60	45.10	36.26	23.97	1.00	0.89	3.89	1.69	0.27	0.71	2.52	2.98	6.64	2.11
V_{EF}	2.22	2.70	5.98	5.28	2.43	1.47	1.75	1.93	2.19	1.84	1.44	2.64	3.10	2.63
Mn/Sr	1.44	1.50	0.93	1.48	3.34	4.18	1.37	2.14	2.39	1.41	1.98	1.51	1.22	1.62
Ba_{bio}/%	379.29	546.51	826.19	581.82	572.17	209.09	429.20	510.02	480.07	492.69	325.05	490.11	549.94	605.36
Stage	2	2	1	1	1	1	1	1	1	1	1	1	1	1
Depth/m	493.10	509.20	518.70	525.10	526.70	541.10	550.70	557.10	558.70	566.70	573.10	581.10	587.10	595.10	603.10
Well-Sample ID	B-18	B-19	B-20	B-21	B-22	B-23	B-24	B-25	B-26	B-27	B-28	B-29	B-30	B-31	B-32
V/ppm	131.95	147.28	145.56	166.94	184.45	182.07	231.84	231.83	298.35	309.51	242.96	166.56	217.98	214.24	302.59
Cr/ppm	189.33	144.17	81.67	112.73	118.59	119.96	101.64	86.64	95.43	164.57	86.87	86.64	109.36	83.49	94.00
U/ppm	4.80	6.00	4.36	8.69	13.25	3.66	3.66	2.36	5.50	13.21	13.20	10.36	5.50	7.03	10.00
Mo/ppm	2.86	5.36	1.36	5.69	4.36	8.99	5.76	3.25	16.35	22.30	9.06	5.36	18.00	11.03	10.09
Ni/ppm	85.26	127.31	115.44	113.43	85.69	117.11	170.06	109.26	132.17	142.16	99.71	86.55	135.95	92.41	138.31
Zn/ppm	60.70	59.19	53.64	30.18	65.91	66.60	99.26	56.64	57.92	96.61	35.90	74.35	52.35	70.25	71.88
Rb/ppm	87.59	71.30	66.76	51.94	86.32	87.92	89.57	89.90	77.96	66.56	93.48	80.33	115.10	81.13	87.95
Sr/ppm	205.29	222.25	344.65	437.62	265.89	191.91	305.17	278.51	294.46	418.21	228.89	220.81	254.94	311.69	212.13
Zr/ppm	90.08	101.17	97.83	65.69	119.62	91.46	110.17	109.24	100.39	88.24	110.83	65.18	105.66	99.16	86.64
Nb/ppm	7.48	9.28	10.13	5.73	9.66	10.39	11.61	10.47	8.05	8.31	9.83	8.12	10.53	7.17	10.50
Ba/ppm	1002.96	862.46	812.54	855.85	962.19	804.65	913.31	949.32	810.58	756.19	877.52	971.18	1151.30	925.00	918.69
Th/ppm	9.16	9.53	8.13	9.96	11.13	9.79	11.58	9.20	10.38	8.06	9.03	7.48	11.79	7.03	6.91
V/Cr	0.70	1.02	1.78	1.48	1.56	1.52	2.28	2.68	3.13	1.88	2.80	1.92	1.99	2.57	3.22
V/(V + Ni)	0.61	0.54	0.56	0.60	0.68	0.61	0.58	0.68	0.69	0.69	0.71	0.66	0.62	0.70	0.69
U_{EF}	2.76	2.45	1.97	3.93	5.59	1.45	1.25	0.93	2.24	6.43	4.91	7.71	2.24	3.18	5.06
Mo_{EF}	2.34	3.11	0.87	3.66	2.62	5.06	2.80	1.83	9.49	15.44	4.80	5.68	10.45	7.09	7.26
V_{EF}	2.38	1.89	2.10	2.40	2.42	2.29	2.49	2.92	3.82	4.71	2.83	3.84	2.85	3.12	4.77
Mn/Sr	0.97	1.35	1.16	0.69	0.75	1.04	0.98	0.72	0.68	0.96	0.87	0.91	0.39	0.64	0.94
Ba_{bio}/%	759.85	421.79	509.55	550.84	629.21	456.90	506.49	602.03	468.78	468.73	501.40	781.26	816.17	624.13	740.89

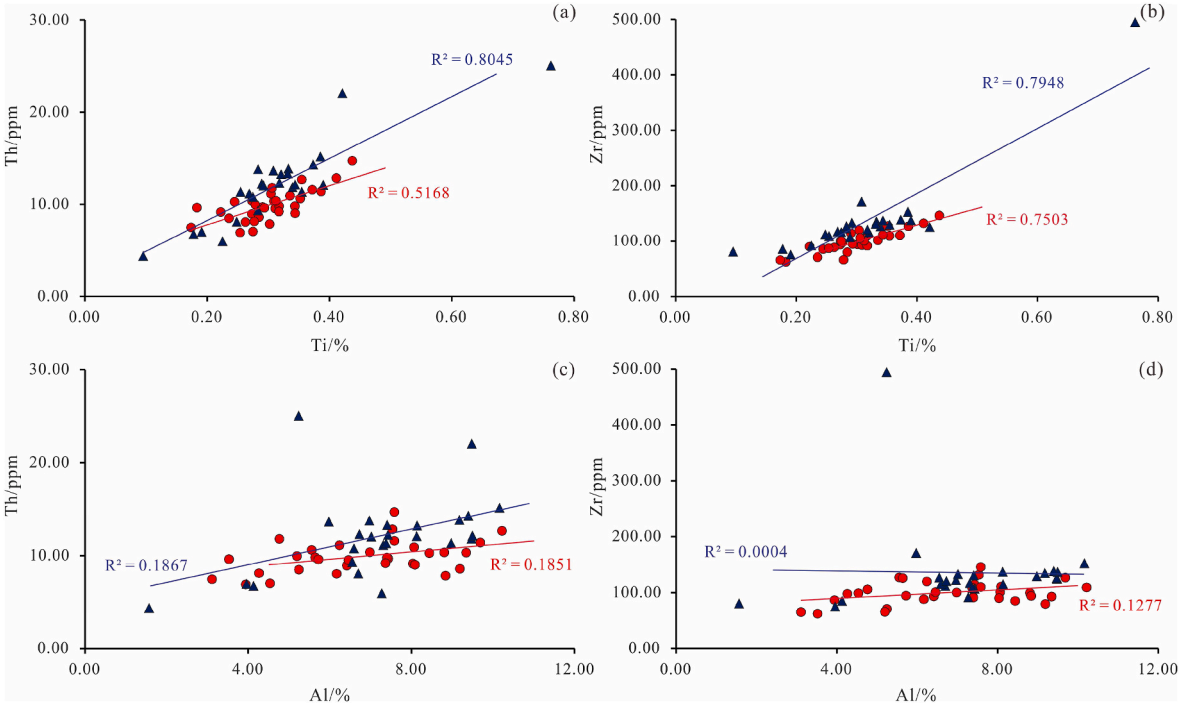

Fig. 11. Cross plots of Ti versus Th (a) and Zr (b), and Al versus Th (c) and Zr (d) (triangles: Well A; circles: Well B).

isolated platforms (Fig. 1c) does not diminish the influx of terrigenous debris in the Baise Rift Zone (Fig. 6a–b). Consequently, the sedimentary deposits within the basin and slope have undergone a significant influence from terrestrial sources, encompassing detrital minerals, organic matter, and other components. As a result, the sediment in the Youjiang Basin has been influenced by terrestrial detrital input during the process of organic matter enrichment.

5.2.1. *Dilution effect*

The correlation between Si/Ti and TOC content of each stage in the A and B wells varies considerably (Fig. 12a–b), suggesting that the dilution degree of TOC by the terrestrial debris varies. Although the correlation between Si/Ti and TOC is slightly positive in stage 2 (R = 0.0354), the correlation between the two is almost always negative for the Luofu Formation samples (with R values at −0.2145 of stage 1, -0.7747 of stage 3 and -0.3759 of stage 4) (Fig. 12a). This suggests that the terrestrial debris diluted the organic matter of Well A. For the samples of Well B, the input of terrestrial debris did not cause the organic matter dilution, as shown by the correlation between Si/Ti and TOC content from stage 1 to stage 4 (with R values at −0.2398, 0.4551, 0.6852 and 1.0000, respectively) (Fig. 12b). This may be related to the input of terrestrial debris into the basin by weathering into clay minerals after a long-distance transport. The degree of organic matter accumulation by clay minerals slightly exceeded the dilution intensity caused by the terrestrial debris input.

5.2.2. *Concentration effect*

(1) Rapid input of terrestrial debris

For Well A, the Ti, Zr and Th contents of stage 4 increase significantly (Fig. 6a). The calcareous mudstone of stage 4 is characterized by a greyish-white color (Fig. 5e), with an abundance of sandy detrital particles (Fig. 4h). The quartz grains observed within detrital sediment exhibit subangular shapes with irregular boundaries and have grain sizes ranging from approximately 10 to 100 μm. These quartz grains are poorly sorted (Fig. 4i). The rapid accumulation of terrestrial detrital particles in a turbulent water environment within broken shells of shallow water columns (Fig. 4h).

The sharp increase in the content of Ti and Zr suggests a strong terrestrial detrital influx of stage 4 in Well A (Fig. 6a). This may result in an accelerated sedimentation rate of mudstone and form a sediment layer in the bottom water columns (Fig. 4h–i). This made it difficult for oxygen and benthic organisms to reach organic matter, thus greatly reducing the rate of organic matter consumption (Summerhayes, 1987; Hedges and Keil, 1995; Wang et al., 2019). At the same time, buried microorganisms may no longer be the first priority of organism, but rather ensure access to the oxygen needed for survival (Canfield, 1994). This can further reduce the rate of organic matter consumption (Ibach, 1982). Therefore, TOC is negatively correlated with V/Cr of the oxic water columns (R = −0.5798) (Fig. 12e).

(2) Formation of organo-mineral complex

The high surface reactivity and colloidal nature of organic matter makes it easy to combine with clay minerals (Kennedy and Wagner, 2011; Li et al., 2020; Zhou et al., 2020; Gu et al., 2023). The study area had obtained a continuous supply of clay minerals from the Yangtze platform (Cheng, 2011b). In conjunction with the gradual deposition of organic matter in the water column, the introduction of significant quantities of clay minerals impedes the oxidation and hydrolysis processes within the sediments (Mansour et al., 2020). As a result, organic matter becomes adsorbed onto the surfaces of clay minerals or enters the interlayers of clay minerals, giving rise to a multitude of organo-mineral complexes (Fig. 8a–f). In these complexes, a considerable portion of organic matter becomes adsorbed onto the inner surfaces of clay minerals, leading to the formation of stable organic carbon (SOC) (Fig. 8a–e). OM associated with SOC is more stable due to the protection of crystal structure and stronger bonding (Playter et al., 2017). At the same time, the symmetrical arrangement of organic matter molecules between clay mineral layers also increases the stability of organo-mineral complexes (Li et al., 2020).

The TOC content shows a positive correlation (R = 0.6177) with clay content of stage 2 in Well B (Fig. 12d), indicating that the input of clay

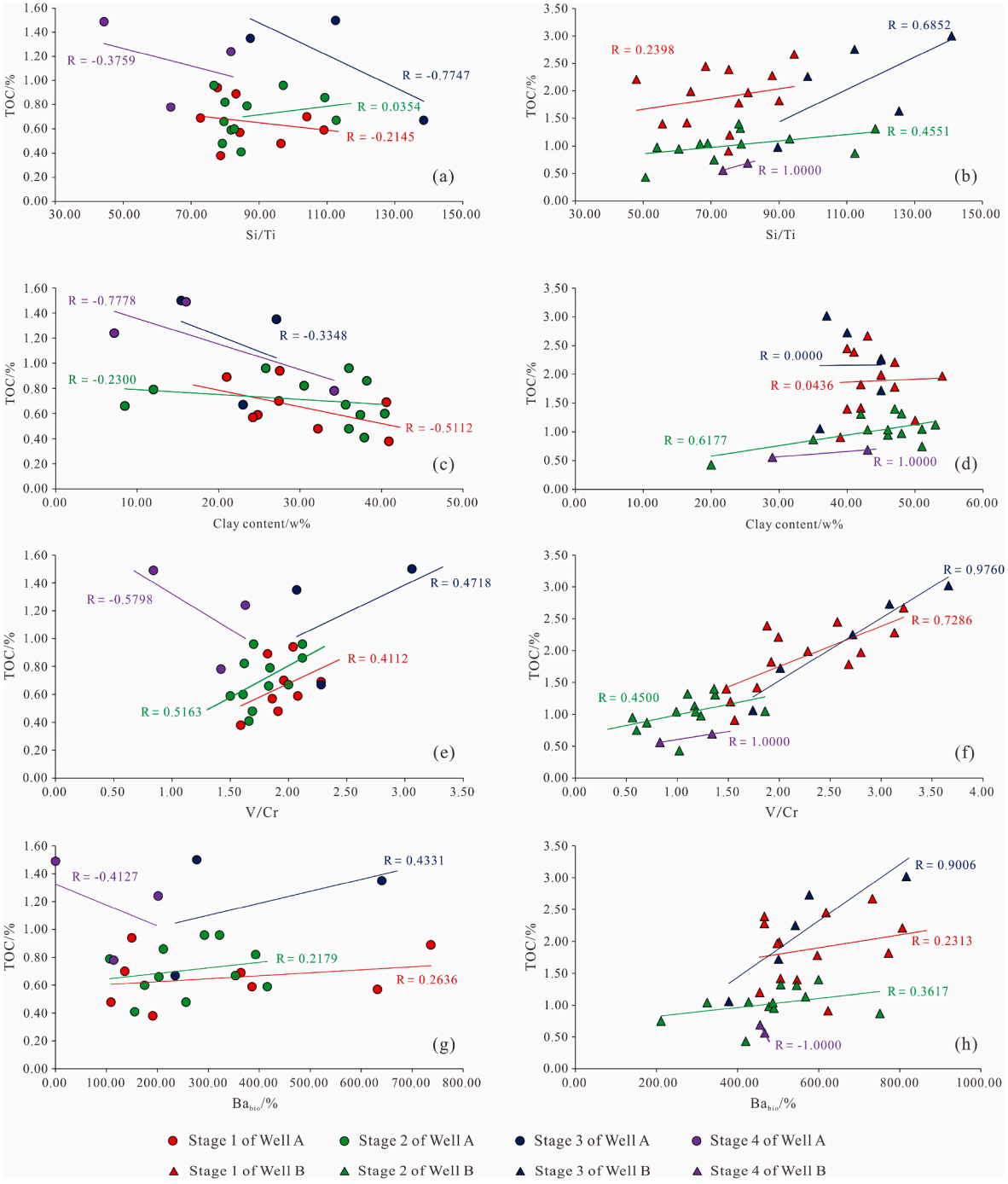

Fig. 12. Cross plots of Si/Ti of Well A (a), Si/Ti of Well B (b), Clay content of Well A (c), Clay content of Well B (d), V/Cr of Well A (e), V/Cr of Well B (f), Ba_{bio} of Well A (g) and Ba_{bio} of Well B (h) versus TOC.

mineral promotes the accumulation of organic matter to some extent. A large number of organic mineral complexes that may have formed during the deposition period are visible in calcareous mudstone with TOC content greater than 1.00%, compared to that with TOC less than 1.00% (Fig. 8d–f). The kerogen macerals of stage 2 show that the kerogen almost belongs to type I (Fig. 7f, Appendix 1), suggesting that the organic matter in the complex originated from marine organisms rather than terrestrial plants. In the calcareous mudstone with TOC content greater than 1%, the organic mineral complexes may be deposited simultaneously with euhedral crystals (Fig. 8f). The fact that both were deposited together reflected the fact that the complexes may have attenuated the decomposition of organic matter by the oxygen-enriched water columns to some extent, thus promoting organic matter accumulation. For the samples of stage 3 in Well A, TOC is negatively correlated with clay content (R = −0.3348), although a large number of complexes are developed (Fig. 8a–c). It is possible that the relatively high productivity and dysoxic water columns promoted the organic matter accumulation, thus masking the promotion of organic matter accumulation by the complexes.

The comparison of clay content and TOC correlations in stage 3 of Well A and stage 2 of Well B suggests that the complexes may promote organic matter accumulation to some extent (Fig. 12c–d), which, however, is only highlighted in the oxic water columns with low productivity and stable terrestrial detrital influx.

5.3. Evolution of paleoredox condition

Redox conditions play a critical role in the degree of organic matter enrichment (Jones and Manning, 1994; Chang et al., 2009; Zheng et al., 2022), with anoxic conditions favoring organic matter preservation and oxic conditions promoting the decomposition of organic matter (Wang et al., 2020). The biomorphic characteristics and the elemental contents will change under different redox conditions (Li et al., 2017; Wang et al., 2019). Thus, the biotypes (Gong and Wu, 1997; Du et al., 2009), pyrite characteristics (Raiswell and Berner, 1985, 1986; Wignall and Newton, 1998), and redox-sensitive element contents (e.g., Mo, U and V) (Arthur and Sageman, 1994; Wu et al., 2020) can be used to reconstruct the redox state of water columns. Algeo and Tribovillard (2009) proposed the use of U_{EF} and Mo_{EF} as indicators to reflect the redox conditions. Under anoxic conditions, the framboidal pyrite is small and highly developed (Wilkin et al., 1996;Mahoney et al., 2019), while in oxic environments pyrite generally does not develop (Wilkin and Barnes, 1997; Wignall et al., 2010). The DOP_T is reported to be < 0.42 for oxic condition, 0.42–0.75 for dysoxic condition, and >0.75 for anoxic condition (Appalachian et al., 2019; Qie et al., 2019). Under reducing conditions, V is mainly deposited through its combination with organic matter in the form of V^{4+}, and Cr^{+6} is reduced to Cr^{3+} (Arthur and Sageman, 1994; Rimmer, 2004). The criteria for V/Cr ratios are <2.00 for oxic condition, 2.00–4.25 for dysoxic condition, >4.25 for anoxic or euxinic environment (Wang et al., 2019). Furthermore, the ratios of V/(V + Ni) in the range of <0.46, 0.46–0.84, and >0.84 reflect oxic conditions, dysoxic conditions, and anoxic conditions, respectively (Arthur and Sageman, 1994; Neumeister et al., 2016).

5.3.1. Deposition of stage 1: diminishing dysoxic water conditions

The redox indicators (DOP_T, V/(V + Ni), V/Cr) of Well B indicate dysoxic bottom-water columns in the basin (Fig. 6b). In the dysoxic water columns, the normal framboid diameters are mainly 4–8 μm, with an average diameter of 6.10–7.98 μm (Fig. 9a–b, 10c-d). There are also a small number of large pyrite framboids (>10 μm) (Fig. 9a–b, 10c-d) and clustered crystals (Fig. 9l). The pattern of U_{EF}-Mo_{EF} suggests that mudstone of Well B was formed under oxic-to- suboxic water columns, and calcareous mudstone of Well A formed under oxic conditions with less enrichment of Mo and U (Fig. 13a–b). In Well A samples, the values of V/Cr and DOP_T also show an oxic water column on the slope (Fig. 6a). The development of parallel bedding and extensive bioclastic levels support a low relative sea-level as well (Fig. 4a). Qie et al. (2019) once reported that the decline of relative sea-level in the Youjiang Basin was caused by the Kacak Event. In the oxic water columns, the normal framboid diameters are highly variable, commonly >8 μm (Fig. 9c–d), with mean 8.30–11.30 μm (Fig. 10a–b). There are also large diameter framboids and overgrown framboids in Well A (Fig. 9i). In summary, a widespread oxic water column was prevalent on the slope, while a dysoxic bottom-water column existed in the basin.

As shown by the correlation between TOC and V/Cr in Well A (R = 0.4112) and Well B (R = 0.7286) (Fig. 12e–f), the dysoxic conditions of stage 1 promote the accumulation of organic matter in the bottom-water columns of the basin.

5.3.2. Deposition of stage 2: wide-spread oxic water conditions

The redox indicators (V/Cr, V/(V + Ni), DOP_T) of Well A (Fig. 6a) suggest an oxic bottom-water condition on the slope. The low values of U_{EF} and Mo_{EF} are also evidence of oxic water columns (Fig. 13a). The parallel bedding was developed in shallow water columns with relatively strong hydrodynamic forces (Fig. 4a). Samples of Well B show low values of V/Cr, V/(V + Ni), V_{EF}, DOP_T (Fig. 6b), U_{EF}, Mo_{EF} (Fig. 13b) and euhedral crystal is visible in all well samples (Fig. 9k, j). Along with the appearance of ripple cross laminated (Fig. 4b), a large number of broken shells and calcite spherules are found in stage 2 (Fig. 4c–e). The observations suggest the presence of high-energy water conditions within the shallow water columns, resulting in the wider distribution of oxygenated water extending from the basin to the slope.

There is a no strong correlation between TOC and V/Cr in the A and B wells (with R values at 0.5163 and 0.4500, respectively) (Fig. 12e–f). This may be related to the large amount of organic matter consumed in oxygen-enriched water columns. The positive correlation between two variables shows that oxic water columns limited the organic matter accumulation of stage 2 (Fig. 12e–f).

5.3.3. Deposition of stage 3: wide-spread dysoxic/anoxic water conditions

Compared to stage 2, 3 samples of stage 3 exhibit obvious enrichment of Mo and U (Table 3). The pattern of U_{EF}-Mo_{EF} suggests that a suboxic-to-anoxic water column (Fig. 12a). The higher concentrations of V/Cr and DOP_T of Well A also suggest a dysoxic water condition on the slope (Fig. 6a). In dysoxic water columns, the calcareous mudstone has a lot of framboidal pyrites with generally 4–8 μm (mean 5.99–6.12 μm) (Fig. 10e, f) and a few clustered crystals (Fig. 9e–f). In Well B, the diameters of most framboidal pyrites are almost 2–6 μm (mean 4.20–4.80 μm) (Fig. 10g and h). The high values of DOP_T, V/Cr, V/(V + Ni) and V_{EF} are observed (Fig. 6b), which may be related to a dysoxic water column. The pattern of U_{EF}-Mo_{EF} suggests that anoxic-to-euxinic water conditions (Fig. 13b), which may be related to the occurrence of more widely spread reducing water columns in the basin. As the transgression progressed (Walliser, 1996; Qie et al., 2019), the basin water columns deepened and became less restricted, as evidenced by the Mo_{EF}/U_{EF} ratios were mostly in the "unrestricted marine trend" (Fig. 12a–b). The siliceous mudstone was deposited over the calcareous mudstone in Well B (Fig. 4g). In summary, the water columns generally deepened throughout the Youjiang Basin. The generally dysoxic water columns are on the slope, and the bottom water columns are generally under anoxic conditions.

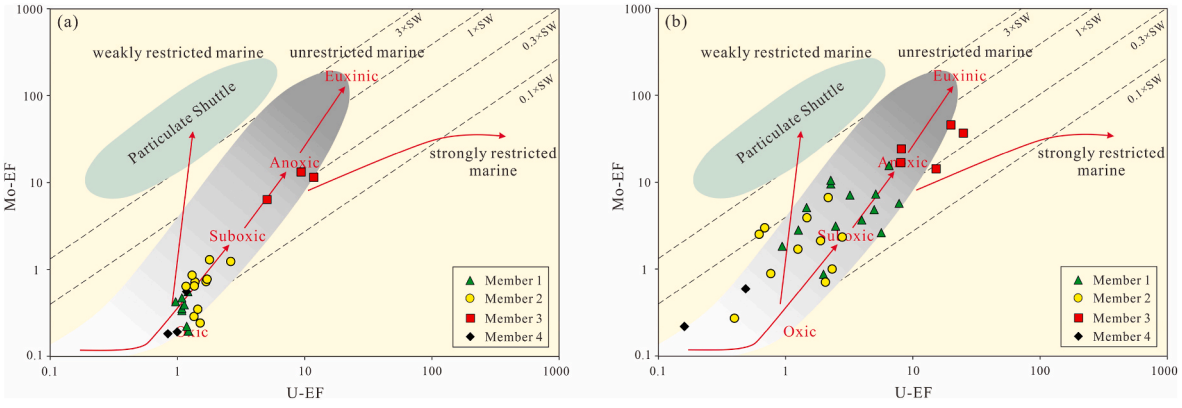

Fig. 13. Covariation pattern of Mo-EF versus U-EF (modified from Tribovillard et al., 2012; Wu et al., 2022).

The correlation between TOC and the redox fingerprint (V/Cr) suggests that both dysoxic (R = 0.4718) and anoxic (R = 0.9760) water columns can promote the organic matter accumulation (Fig. 12e–f). In particular, the anoxic bottom water columns in the basin greatly contributed to the organic matter enrichment (Fig. 12f).

5.3.4. Deposition of stage 4: wide-spread oxic water conditions

The low values of both wells (DOP_T, V/Cr, δU) show oxic water conditions (Fig. 6a–b). This is supported by the pattern of U_{EF}-Mo_{EF} (Fig. 13a–b). There is also an absence of framboidal pyrites in all the samples. These observations suggest the presence of an oxic environment. From the basin towards the slope, there is a distinct rise in carbonate content of the sediment, with argillaceous limestone becoming increasingly prevalent (Fig. 4m). Calcite spherules and benthic organisms proliferate in the shallow columns, leaving abundant skeletal materials (Fig. 4m). During this stage, the study area experienced a gradual expansion of oxic water columns overlaying it (Fig. 4i).

The organic matter was preserved at shortened exposure duration of oxic water columns, leading to a negative correlation between TOC and V/Cr of Well A (R = −0.5798) (Fig. 12e). Although the correlation between TOC and V/Cr of Well B is positive (R = 1.0000) (Fig. 12f), the oxic water columns consumed organic matter, resulting in generally low TOC content.

5.4. Paleoproductivity

Paleoproductivity is a concept that refers to the amount of organic matter produced by organisms in a given area and time during the energy cycle (Wang et al., 2020; Xiao et al., 2021). High productivity can provide abundant organic matter, and thus promote organic matter enrichment. Additionally, high productivity consumes more oxygen in the water columns, further promoting an anoxic environment that facilitates the preservation of organic matter (Li et al., 2017; Wang et al., 2019). Some factors, including the impact of water level, the type of water column (i.e., upwelling, downwelling, density-stratified water column), and role of terrestrial organic matter supply, have had significant impact on the paleoproductivity conditions (Mansour and Wagreich, 2022). Nonetheless, establishing past productivity levels can be complicated given the unequal dispersion of nutrients like carbon, nitrogen, phosphorus, and barium in the marine ecosystem (Calvert and Pedersen, 2007; Schoepfer et al., 2015; Li et al., 2017). Therefore, the results of paleoproductivity need to be confirmed by multiple indicators.

The barium concentration in marine sediments mainly originates from biogenic, terrestrial debris, and carbonate lattices (Schoepfer et al., 2015). Once organisms in the marine ecosystem die, their bio-barium becomes combined with sulfate in the surrounding seawater, resulting in the preservation of bio-barium in the form of barite (Schoepfer et al., 2015). Thus, Ba_{bio} content is used for determining the level of paleoproductivity. The typically higher productivity of Well B compared to Well A is reflected in the fact that Well B typically has higher Ba content than Well A dose (Fig. 6a–b). The Ba_{bio} content of both wells is lower than 1000 ppm, which is also much lower than the productivity of marine mudstone such as the Wufeng-Longmaxi Formation (Wang et al., 2020; Xiao et al., 2021). The generally low productivity may be one of the reasons for the widespread development of organic-poor mudstone in the Youjiang Basin.

There are various sources of silicon in sediments, of which only biologically derived silicon represents paleoproductivity (Calvert and Pedersen, 2007; Xiao et al., 2021). Biological activities and volcanic hydrothermal fluids strongly influence the supply of biogenic silica. The Al–Fe–Mn ternary diagram indicates no significant hydrothermal activity during deposition (Fig. 14a–b). Therefore, the Si_{bio} content can accurately reflect the level of paleoproductivity. The Si_{bio} content of Well B is generally higher than that of Well A. This is consistent with what the Ba content suggests, indicating presently higher productivity levels in Well B than in Well A. In Well A, the Si_{bio} content shows a trend of first increasing and then decreasing from stage 1 to stage 4 (Fig. 6a). Stage 3 has relatively high Si_{bio} content, indicating higher productivity compared to the other stages. While in Well B, stage 3 has relatively high Si_{bio} content as far as the Luofu Formation mudstone is concerned (Fig. 6b), indicating relatively high level of productivity in stage 3.

Previous studies have demonstrated the effectiveness of using the ratios of Ni/Ti and Zn/Ti to characterize paleoproductivity, due to their excellent enrichment within organic matter by the form of complexes after organic matter decay, as proposed by Böning et al. (2004) and Tribovillard et al. (2006). In Well A, stage 4 and stage 2 both have low values of Ni/Ti and Zn/Ti, indicating a low level of productivity (Fig. 6a). This may be related to a decrease in the level of algal development, as evidenced by the reduction of sapropelinite (Fig. 7b and c). The values of Ni/Ti and Zn/Ti are significantly increased in stage 3 of Well B (Fig. 6b). As shown in Fig. 7a, d, e, the large increase in sapropelinite content indicates that algal blooms are responsible for the increase in the concentrations of Ni and Zn.

For the samples of Well A, the oxic water columns consume part of organic matter, leading to poor correlation between TOC and Ba_{bio} of stage 1 (R = 0.2636) and stage 2 (R = 0.2179) (Fig. 12g). Compared to stages 1 and 2, TOC content of stage 3 was not consumed by the dysoxic water columns. The correlation between TOC and Ba_{bio} shows that productivity contributes to some extent to the organic matter accumulation (R = 0.4331) (Fig. 12g). In stage 4, the input of terrestrial plant debris associated with mineral debris had allowed much vitrinite to be in kerogen (Fig. 7c; Appendix 1), resulting in an increase in TOC content, but the productivity indicator (Ba_{bio}) failed to record this change (R = −0.4127) (Fig. 12g). For the samples of Well B, although there is a positive correlation between TOC and Ba_{bio} content in stage 1 (R = 0.2313), stage 2 (R = 0.3617) and stage 3 (R = 0.9006), only the correlation in stage 3 between the two is high (Fig. 12h), suggesting that the productivity of stage 3 contributed significantly to the organic matter enrichment. For samples of stage 4, the oxic water columns consumed organic matter, which masked the contribution of productivity to TOC

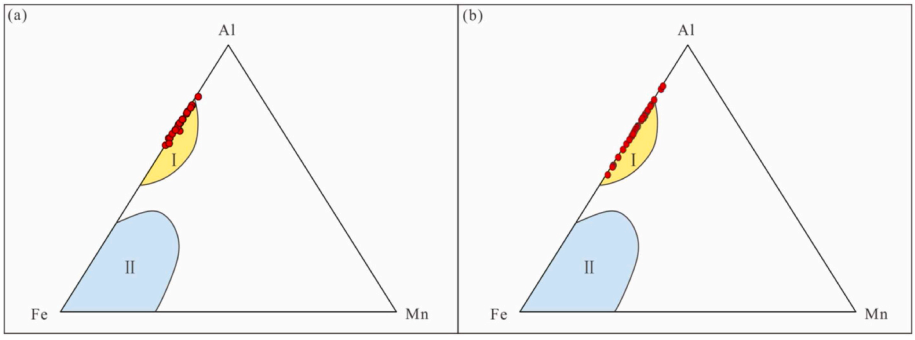

Fig. 14. The ternary diagram of Al–Fe–Mn showing all samples of Well A (a) and Well B (b) falling into the biogenic and non-hydrothermal area. I: biogenic and non-hydrothermal sediments, II: hydrothermal sediments. Hydrothermal and non-hydrothermal fields are from Zhang et al. (2020) and Wei et al. (2022).

content (Fig. 12h).

5.5. Controlling factors of the organic matter accumulation

The correlation of each stage observed between different geochemical indicators, such as redox, paleoproductivity, and terrestrial debris flux, with TOC content indicates that organic-poor mudstone (TOC <1.00%) was deposited in the oxic water columns, such as stage 1 and stage 2 of Well A, and stage 2 and stage 4 of Well B. Firstly, the oxic water columns may be related to the relatively low sea-level (Gong et al., 1994; Jarvis et al., 2001). The Kacak Event caused uplift in parts of southern China, which weakened the transgression intensity (Walliser, 1996; Qie et al., 2019) and resulted the relatively low sea-level in the Youjiang Basin. Secondly, siliceous masses and layers of the Middle Devonian are associated with upwelling (Gong and Wu, 1997; Du et al., 2009). In confined basins, upwelling conditions may enhance water column ventilation, thereby increasing the amount of dissolved oxygen in the water columns (Mansour and Wagreich, 2022). Thirdly, abundant dissolved O_2 and carbonate fractions can lead to significant oxidization/distortion and dilution of labile organic matter ($2CH_2O$) (Ricken, 1996; Mansour and Wagreich, 2022).

Meanwhile, the low productivity water columns limit the deposition of more organic-rich mudstone (TOC >2.00%) in dysoxic/anoxic water columns (Pedersen and Calvert, 1990; Mansour and Wagreich, 2022). The complexity of these interactions is further compounded by the fact that low productivity is also a factor that restricts the accumulation of organic matter in the Luofu Formation. Firstly, the low productivity was influenced by various factors, such as the progressive lowering of planktonic algae that could serve as primary hydrocarbon-producing organisms. The lack of planktonic algae may be due to the restricted supply of marine nutrients, caused by poor exchange of the shallow water columns of the archipelago with active seawater circulation pattern (Pan et al., 2020; Mansour and Wagreich, 2022). Lower nutrient availability had led to a decrease in the number of bacteria and algae, and coral-laminar foraminifera bloomed (Algeo and Scheckler, 1998; Wu et al., 2013). Secondly, the absence of submarine hydrothermal activity in the Nandan area (location of Well A) (Wang et al., 2018) and Baise area (location of Well B) (Yuan et al., 2020) exacerbated the deficiency of nutrient elements, which severely limited the development of organisms and productivity. In contrast, the hydrothermal activities of areas Badu (Huang et al., 2013), Siding (Schneider et al., 1991), and Dachang (Ju et al., 2011) all contributed to some extent to the development of the Middle Devonian organic-rich mudstone (TOC >2.00%) in the Youjiang Basin.

Although the Luofu Formation has relatively low TOC content, it still possessed the essential conditions for source rock formation. The deposition of organic-containing mudstone (2.00% > TOC >1.00%) is facilitated by the relatively high productivity and dysoxic water columns, such as stage 3 of Well A. The development of organic-rich mudstone (TOC >2.00%) in this formation can be attributed to high productivity and dysoxic/anoxic water columns, like stage 1 and stage 3 of Well B. Therefore, it can be inferred that organic-rich mudstone was deposited in the bottom water columns of the basin away from upwelling and probably close to hydrothermal activity. Compared to other stages of the Luofu Formation, stage 3 had wide distribution of anoxic water columns, high productivity, and a stable terrestrial debris flux, thus becoming the main stratum for organic-rich mudstone exploration.

5.6. Model of organic matter accumulation

On the basis of comparing the depositional locations and environmental differences between organic-rich mudstone, organic-containing mudstone and organic-poor mudstone, and by analyzing the redox conditions, productivity, and terrestrial detrital influx results of each stage, we propose an integrated environmental and organic matter accumulation model in the archipelagic marine.

At the beginning of the Givetian Stage, the Kacak Event caused an uplift in parts of southern China and led to sea-level regression (Walliser, 1996; Qie et al., 2019). The redox indicators of the A and B wells (DOP_T and V/Cr) suggests that an oxygen-rich water column in the slope and a dysoxic condition in a basin bottom water column (Fig. 6a–b). The oxic water columns of Well A exacerbated the rate of organic matter depletion (Fig. 12e), while the dysoxic conditions of the basin bottom water columns in Well B contributed to the aggregation of organic matter (Fig. 12f). The values of Ba_{bio} and Si_{bio} show that the productivity of Well A gradually declined to a low level, which was consistent with the near-zero $\delta^{13}C_{carb}$ values (Fig. 6a). For samples of Well B, there was almost no change in productivity (Fig. 6b). However, the weak correlation between the productivity indicators and TOC content indicates that the organic matter accumulation was not related to productivity during this stage (Fig. 12g–h). The terrestrial detritus input acted as dilution of organic matter, which was more pronounced on Well A (Fig. 12a–b). The organic matter was almost exclusively derived from sapropelinite in kerogen (Appendix 1). In stage 1, the dysoxic conditions are responsible for the organic matter accumulation in the basin bottom water columns (Fig. 15a).

The values of Ba_{bio} and Si_{bio} suggest low productivity of Well A, which was consistent with the near-zero $\delta^{13}C_{carb}$ values (Fig. 6a). Although the productivity of Well B is slightly higher than that of Well A (Fig. 6a–b), the oxic water columns have a negative effect on the accumulation of organic matter (Fig. 12e–f). The input of terrigenous debris diluted the organic matter of Well A (Fig. 12a, c). The sapropelinite in kerogen was the main source of organic matter in stage 2 (Appendix 1). Although the organo-mineral complexes may contribute somewhat to the deposition of organic-containing mudstone in Well B (Fig. 8d–f, 12b, d), organic-poor mudstone was developed from the slope to the basin in the oxic water columns with low productivity (Fig. 15b).

In stage 3, the bottom water columns from the basin to the slope was in reducing conditions (Fig. 6a–b). This may be related to the deepening of the water columns as a result of the Taghanic Transgression Event (Walliser, 1996; Qie et al., 2019). The correlations of redox indicators (V/Cr) and TOC content show that dysoxic/anoxic conditions contributed to the organic matter enrichment, with more significant contribution of anoxic water columns (Fig. 12e–f). The values of productivity indictors show an increase in productivity from basin to slope, which were recorded by the values of Ba_{bio}, Ni/Ti, Zn/Ti and $\delta^{13}C_{carb}$ (Fig. 6a–b), while the productivity on the slope continues to be low (Fig. 6a–b). The correlation between the values of Ba_{bio} and TOC content shows that productivity greatly contributed to the organic matter enrichment of the basin bottom water columns (Fig. 12g), and promoted to some extent the deposition of organic-containing mudstone on the slope (Fig. 12h). The terrestrial detrital influxes of the A and B wells were stable (Fig. 6a–b). Although clay minerals combined with organic matter on the slope form complexes (Fig. 8a–c), the contribution of complexes to organic matter accumulation was extremely limited (Fig. 12c). The terrestrial detrital flux manifested itself more as dilution of organic matter provided by sapropelinite (Fig. 12a–b) (Appendix 1). In summary, the development of organic-containing and organic-rich mudstones benefited from the dysoxic/anoxic conditions and relatively high productivity (Fig. 15c).

The redox indicators (DOP_T, V/Cr and δU) of stage 4 show that the oxic water columns were widely distributed from the basin to the slope (Fig. 6a–b), which were unfavorable for the accumulation of organic matter (Fig. 12e–f). Also, the productivity did not contribute to the organic matter accumulation within the basin and slope, as shown by the lack of positive correlations between the productivity and TOC content (Fig. 12g–h). As a result, a large amount of organic-poor mudstone was deposited in the basin. Syn-sedimentary faults were frequently active in the Givetian period (Mei et al., 2007; Yang et al., 2020), making the slope susceptible to large input of terrestrial debris in a short time and the higher plants brought along with it were rapidly buried. This resulted in the source of organic matter not only from sapropelinite, but

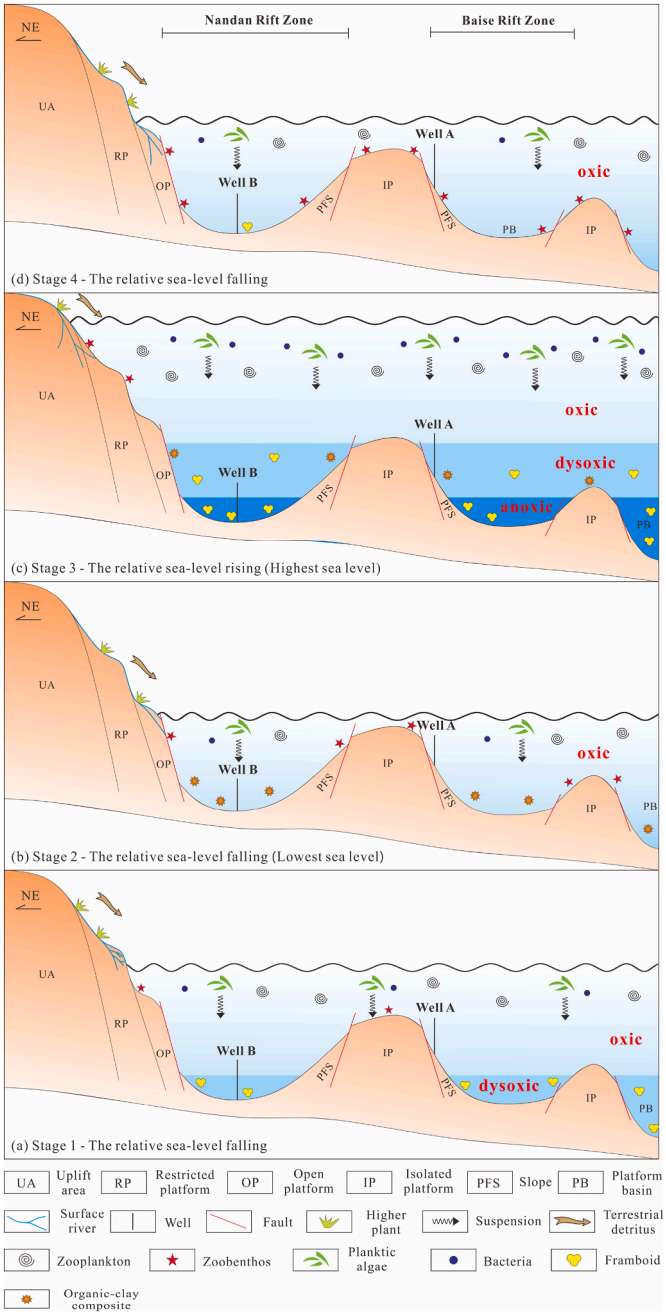

Fig. 15. Models of organic matter accumulation in the middle Devonian Givetian Luofu Formation sediments in the Youjiang Basin during the deposition of stage 1 (a), stage 2 (b), stage 3 (c), and stage 4 (d).

also from vitrinite (Appendix 1). The increased sedimentation rate shortened the kerogen exposure time in the oxic water columns, leading to a moderate organic matter enrichment, and thus organic-containing mudstone (Fig. 15d).

6. Conclusions

A large amount of work and data have been done, and the following conclusions can be drawn.

(1) The carbonaceous and siliceous mudstones of siliceous lithofacies were developed in the basin of deep-water columns. The calcareous mudstone of mixed lithofacies was deposited in the slope of shallow-water columns.

(2) In the Luofu Formation, the organic-poor mudstone (TOC <1.00%) was deposited in the oxic water columns with low productivity. The deposition of organic-containing mudstone (2.00% > TOC >1.00%) was partly facilitated by the organo-mineral complexes formed during the sedimentary period in the basin and a brief period of exposure on the slope under oxic conditions. The development of organic-rich mudstone (TOC >2.00%) attributed to dysoxic/anoxic water columns with high productivity.

(3) The main reason for the limited deposition of organic-rich mudstone in the Luofu Formation was oxic water columns and low productivity. The oxygen-enriched water columns were influenced by three factors. Firstly, the relative sea-level was low. Secondly, upwelling increased the amount of dissolved oxygen in the water columns. Thirdly, abundant dissolved O_2 and carbonate fractions led to significant oxidization/distortion and dilution of labile organic matter. The low productivity was influenced by two factors. Firstly, there was a small amount of primary hydrocarbon-producing organisms. The second reason was the absence of submarine hydrothermal activity.

(4) The organic matter accumulation model of Luofu Formation mudstone can be divided into four stages. The organic matter accumulation was caused by the relatively high productivity and dysoxic basin bottom water columns in stage 1. In stage 2, the organo-mineral complexes may promote the organic matter accumulation to some extent in the basin. In stage 3, the organic matter enrichment was facilitated by the dysoxic/anoxic conditions and relatively high productivity from the basin to the slope. In stage 4, the organic matter was preserved on the slope under the shortened exposure duration of oxic conditions.

CRediT authorship contribution statement

Yuzuo Liu: Formal analysis, Methodology, Writing – original draft. **Wanzhong Shi:** Funding acquisition, Project administration. **Qinhong Hu:** Writing – review & editing. **Kun Yuan:** Data curation, Resources. **Xiaofeng Xu:** Writing – review & editing. **Xiaoming Zhang:** Writing – review & editing. **Ren Wang:** Writing – review & editing. **Xianglin Chen:** Writing – review & editing. **Luheng Bai:** Writing – review & editing. **Murray K. Gingras:** Writing – review & editing. **Kurt O. Konhauser:** Writing – review & editing.

Declaration of competing interest

The authors declare that they have no known competing financial interests or personal relationships that could have appeared to influence the work reported in this paper.

Data availability

Data will be made available on request.

Acknowledgments

We thank anonymous reviewers for their constructive comments that greatly improved this manuscript. This study was jointly supported by the China Scholarship Council (CSC) (202206410022), the National Natural Science Foundation of China (No. 41672134), the National Natural Science Foundation of China (No. 42202121), and the fellowship of China Postdoctoral Science Foundation (No. 2022M712952).

Appendix 1

Kerogen maceral analysis results of the Luofu Formation samples from Well A and Well B in the Youjiang Basin.

Stage	Depth/m	Well-Sample ID	Sapropelinite/%	Exinite/%	Vitrinite/%	Inertinite/%	TI	Kerogen type
4	999.30	A-1	63.00	6.00	31.00	0.00	42.75	II_1
4	1026.04	A-2	70.30	1.00	28.70	0.00	49.28	II_1
4	1063.60	A-3	66.50	5.00	28.50	0.00	47.63	II_1
3	1100.10	A-4	96.80	0.00	3.20	0.00	94.40	I
3	1121.60	A-5	99.80	0.00	0.20	0.00	99.65	I
3	1141.40	A-6	97.50	0.00	2.50	0.00	95.63	I
2	1154.40	A-7	90.25	0.00	9.75	0.00	82.94	I
2	1165.50	A-8	88.50	0.00	11.50	0.00	79.88	II_1
2	1178.40	A-9	89.60	0.00	10.40	0.00	81.80	I
2	1185.60	A-10	90.63	0.00	9.37	0.00	83.60	I
2	1203.60	A-11	92.00	0.00	8.00	0.00	86.00	I
2	1222.20	A-12	91.30	0.00	8.70	0.00	84.78	I
2	1235.90	A-13	88.50	0.00	11.50	0.00	79.88	II_1
2	1255.30	A-14	89.60	0.00	10.40	0.00	81.80	I
2	1267.90	A-15	90.20	0.00	9.80	0.00	82.85	I
2	1279.10	A-16	70.00	0.00	30.00	0.00	47.50	II_1
2	1298.40	A-17	90.00	0.00	10.00	0.00	82.50	I
1	1311.40	A-18	91.50	0.00	8.50	0.00	85.13	I
1	1332.20	A-19	89.60	0.00	10.40	0.00	81.80	I
1	1350.40	A-20	91.00	0.00	9.00	0.00	84.25	I
1	1361.15	A-21	90.50	0.00	9.50	0.00	83.38	I
1	1376.20	A-22	91.00	0.00	9.00	0.00	84.25	I
1	1396.40	A-23	90.00	0.00	10.00	0.00	82.50	I
1	1406.00	A-24	93.00	0.00	7.00	0.00	87.75	I
1	1414.60	A-25	92.50	0.00	7.50	0.00	86.88	I
4	331.50	B-1	75.00	3.00	22.00	0.00	60.00	II_1
4	350.10	B-2	89.50	0.00	10.50	0.00	81.63	I
3	377.30	B-3	98.00	0.00	2.00	0.00	96.50	I
3	390.10	B-4	99.00	0.00	1.00	0.00	98.25	I
3	393.30	B-5	99.50	0.00	0.50	0.00	99.13	I
3	401.30	B-6	98.50	0.00	1.50	0.00	97.38	I
3	402.90	B-7	98.00	0.00	2.00	0.00	96.50	I
2	415.70	B-8	90.50	0.00	9.50	0.00	83.38	I
2	417.30	B-9	92.00	0.00	8.00	0.00	86.00	I
2	426.90	B-10	90.00	0.00	10.00	0.00	82.50	I
2	431.10	B-11	91.00	0.00	9.00	0.00	84.25	I
2	435.30	B-12	79.00	0.00	21.00	0.00	63.25	II_1
2	444.90	B-13	90.50	0.00	9.50	0.00	83.38	I
2	451.30	B-14	90.00	0.00	10.00	0.00	82.50	I
2	467.30	B-15	95.00	0.00	5.00	0.00	91.25	I
2	468.90	B-16	95.00	0.00	5.00	0.00	91.25	I
2	476.90	B-17	93.50	0.00	6.50	0.00	88.63	I
2	493.10	B-18	89.00	0.00	11.00	0.00	80.75	I
2	509.20	B-19	92.50	0.00	7.50	0.00	86.88	I
1	518.70	B-20	90.00	0.00	10.00	0.00	82.50	I
1	525.10	B-21	90.50	0.00	9.50	0.00	83.38	I
1	526.70	B-22	91.50	0.00	8.50	0.00	85.13	I
1	541.10	B-23	93.00	0.00	7.00	0.00	87.75	I
1	550.70	B-24	95.00	0.00	5.00	0.00	91.25	II_1
1	557.10	B-25	93.00	0.00	7.00	0.00	87.75	II_1
1	558.70	B-26	92.00	0.00	8.00	0.00	86.00	I
1	566.70	B-27	93.50	0.00	6.50	0.00	88.63	I
1	573.10	B-28	90.50	0.00	9.50	0.00	83.38	I
1	581.10	B-29	90.00	0.00	10.00	0.00	82.50	I
1	587.10	B-30	93.00	0.00	7.00	0.00	87.75	I
1	595.10	B-31	92.00	0.00	8.00	0.00	86.00	I
1	603.10	B −32	90.50	0.00	9.50	0.00	83.38	I

References

Abouelresh, M.O., Slatt, R.M., 2012. Lithofacies and sequence stratigraphy of the Barnett shale in east-central fort worth basin, Texas. AAPG (Am. Assoc. Pet. Geol.) Bull. 96, 1–22.

Algeo, T.J., Maynard, J.B., 2004. Trace-element behavior and redox facies in core shales of Upper Pennsylvanian Kansas-type cyclothems. Chem. Geol. 206, 289–318.

Algeo, T.J., Tribovillard, N., 2009. Environmental analysis of paleoceanographic systems based on molybdenum–uranium covariation. Chem. Geol. 268 (3–4), 211–225.

Algeo, T.J., Scheckler, S.E., 1998. Terrestrial-marine teleconnections in the Devonian: links between the evolution of land plants, weathering processes, and marine anoxic events. Phil. Trans. Roy. Soc. Lond. B Biol. Sci. 353 (1365), 113–130.

Appalachian, C., Liu, J., Algeo, T.J., Jaminski, J., Kuhn, T., Joachimski, M.M., 2019. Evaluation of high-frequency paleoenvironmental variation using an optimized cyclostratigraphic framework: example for C-S-Fe analysis of. Chem. Geol. 525, 303–320.

Arthur, M., Sageman, B.B., 1994. Marine Shales: depositional mechanisms and environments of ancient deposits. Annu. Rev. Earth Planet Sci. 22, 499–551.

Böning, P., Brumsack, H.J., Böttcher, M.E., Schnetger, B., Kriete, C., Kallmeyer, J., Borchers, S.L., 2004. Geochemistry of Peruvian near-surface sediments. Geochem. Cosmochim. Acta 68, 4429–4451.
Brett, C.E., Goodman, W.M., LoDuca, S.T., 1990. Sequences, cycles, and basin dynamics in the Silurian of the appalachian foreland basin. Sediment. Geol. 69, 191–244.
Calvert, S.E., Pederson, T.F., 1992. Organic carbon accumulation and preservation in marine sediments: how important is anoxia? In: Whelan, J.K., Farrington, J.W. (Eds.), Productivity, Accumulation and Preservation of Organic Matter in Modern and Ancient Sediments. University Press, New York, pp. 231–263.
Calvert, S.E., Pedersen, T.F., 2007. Elemental proxies for palaeoclimatic and palaeoceanographic variability in marine sediments: interpretation and application. Developments in Marine Geology 1, 567–644.
Canfield, D.E., 1994. Factors influencing organic carbon preservation in marine sediments. Chem. Geol. 114 (3–4), 315–329.
Chabalala, V.P., Wagner, N., Malumbazo, N., Eble, C.F., 2020. Geochemistry and organic petrology of the permian whitehill formation, Karoo Basin (RSA) and the Devonian/Carboniferous shale of the Appalachian Basin (USA). Int. J. Coal Geol. 232, 103612.
Chang, H.J., Chu, X.L., Feng, L.J., Huang, J., Zhang, Q.R., 2009. Redox sensitive trace elements as paleoenvironments proxies. Geol. Rev. 55 (1), 91–99.
Chen, H.D., Hou, M.C., Lin, L., 2010. Research idea and practice of tectonic-sequence lithofacies paleogeographic in diverse scales. Acta Sedimentol. Sin. 28 (5), 894–905 (in Chinese with English abstract).
Cheng, Y.S., 2011a. Ore-controlling characteristics of Devonian stratum in the Dachang Sn ore-field, Guangxi (south China). Procedia Earth and Planetary Science 2, 28–33.
Cheng, Y.S., 2011b. REE geochemistry of Devonian stratum, in the Dachang ore district, Guangxi, south China. Procedia Earth and Planetary Science 2, 104–108.
Du, Y.S., Gong, Y.M., Liu, B.P., Feng, Q.L., Wu, Y., 1996. Devonian sequence stratigraphy and sea-level changes within the South China Plate. Lithofacies Palaeogeography 16 (6), 14–23 (in Chinese with English abstract).
Du, Y.S., Gong, Y.M., Wu, Y., Feng, Q.L., Liu, B.P., 1997. Devonian sequence stratigraphy and formation and evolution of intraplatform rift trough in the Guangxi and Guizhou Area, China. Acta Sedimentol. Sin. 15 (4), 11–17 (in Chinese with English abstract).
Du, Y.S., Gong, Y.M., Zhang, Z., Zeng, X.W., 2009. Paleoxygenation facies and oxygen-deficient environmental model of the Devonian source rocks from southern South China Sea: an example from the Middle and Upper Devonian of Guangxi. J. Palaeogeogr. 11 (1), 28–36 (in Chinese with English abstract).
Fan, D.L., Zhang, T., Ye, J., Pasava, J., Kribek, B., Dobes, P., Varrin, I., Zak, K., 2004. Geochemistry and origin of tin-polymetallic sulfide deposits hosted by the Devonian black shale series near Dachang. Ore Geol. Rev. 24, 103–120.
Golonka, J., 2002. Plate-Tectonic Maps of the Phanerozoic. Phanerozoic Reef Patterns.
Gong, Y.M., Wu, Y., 1997. The Devonian sea-level change rhythms in south China and coupling relationships of the spheres of the earth. Acta Geol. Sin. 71 (3), 212–226 (in Chinese with English abstract).
Gong, Y.M., Wu, Y., Du, Y.S., 1994. Devonian sequence stratigraphy and frequencies, amplitudes, velocities and phases of sea-level changes in Guizhou and Guangxi provinces (in Chinese with English abstract), 19 (5), 576–586.
Gradstein, F.M., 2020. Evolution and Biostratigraphy. In: Geologic Time Scale 2020. Elsevier, pp. 35–137.
Gu, Y.T., Wan, Q., Li, X.X., Han, T., Yang, S.G., Hu, Q.H., 2023. Structure and evolution of clay-organic nanocomposites in three leading shales in China. J. Earth Sci. 34 (3), 1–14.
Heath, M.N., Cramer, B.D., Stolfus, B.M., Barnes, G.L., Clark, R.J., Day, J.E., Barnett, B. A., Witzke, B.J., Hogancamp, N.J., Tassier-Surine, S., 2021. Chemoautotrophy as the driver of decoupled organic and carbonate carbon isotope records at the onset of the Hangenberg (Devonian-Carboniferous Boundary) Oceanic Anoxic Event. Palaeogeogr. Palaeoclimatol. Palaeoecol. 577, 110540.
Hedges, J.I., Keil, R.G., 1995. Sedimentary organic matter preservation: an assessment and speculative synthesis. Mar. Chem. 49 (2–3), 81–115.
Hou, H.H., Shao, L.Y., Li, Y.H., Liu, L., Liang, G.D., Zhang, W.L., Wang, X.T., Wang, W.C., 2022. Effect of paleoclimate and paleoenvironment on organic matter accumulation in lacustrine shale: constraints from lithofacies and element geochemistry in the northern Qaidam Basin, NW China. J. Petrol. Sci. Eng. 208, 109350.
Hu, D.P., Zhang, X.L., Li, M.H., Xu, Y.L., Shen, Y.N., 2021. Carbon isotope (δ13Ccarb) stratigraphy of the lower-upper ordovician of the Yangtze platform, south China: implications for global correlation and the great ordovician Biodiversification event (GOBE). Global Planet. Change 203, 103546.
Huang, H., Du, Y.S., Huang, Z.Q., Yang, J.H., Huang, H.W., Xie, C.X., Hu, L.S., 2013. Depositional chemistry of chert during late Paleozoic from western Guangxi and its implication for the tectonic evolution of the Youjiang Basin. Sci. China Earth Sci. 56, 479–493.
Huang, J.Y., Liang, K., Wang, Yue, Liao, W.H., Guo, W., Kershaw, S., Jeon, J., Qiao, L., Song, J.J., Ma, Junye, Li, Y., Tu, B., Tian, Y., Wang, Y.J., Wang, Y., Ma, J.X., Luo, M., Qie, W.K., 2020. The Jiwozhai patch reef: a palaeobiodiversity hotspot in middle Givetian (Devonian) of South China. Palaeogeogr. Palaeoclimatol. Palaeoecol. 556.
Ibach, L.E.J., 1982. Relationship between sedimentation rate and total organic carbon content in ancient marine sediments. AAPG (Am. Assoc. Pet. Geol.) Bull. 66 (2), 170–188.
International Committee for Coal and Organic Petrology (ICCP), 1998. The new vitrinite classification (ICCP systems 1994). Fuel 77, 349–358.
International Committee for Coal and Organic Petrology (ICCP), 2001. The new inertinite classification (ICCP system 1994). Fuel 80 (4), 459–471.
Jarvis, I.A.N., Murphy, A.M., Gale, A.S., 2001. Geochemistry of pelagic and hemipelagic carbonates: criteria for identifying systems tracts and sea-level change. J. Geol. Soc. 158 (4), 685–696.
Jones, B., Manning, D.A.C., 1994. A comparison and correlation of different geochemical indices used for the interpretation of depositional environments in ancient mudstones. Chem. Geol. 111 (1–4), 111–129.
Ju, M.H., Zhao, C.B., Dai, T.G., Yang, J.W., 2011. Finite element modeling of pore-fluid flow in the Dachang ore district, Guangxi, China: implications for hydrothermal mineralization. Geosci. Front. 2 (3), 463–474.
Kennedy, M.J., Wagner, T., 2011. A clay mineral continental amplifier for marine carbon sequestration in a greenhouse ocean. Proc. Natl. Acad. Sci. USA 108 (24), 9776–9781.
LaGrange, M.T., Konhauser, K.O., Catuneanu, O., Harris, B.S., Playter, T.L., Gingras, M. K., 2020. Sequence stratigraphy in organic-rich marine mudstone successions using chemostratigraphic datasets. Earth Sci. Rev. 203, 16, 103137.
Li, X.X., Gu, Y.T., Wan, Q., Yang, S.G., 2020. Research advance on microstructures of the organo-mineral complex in mud shale. Bull. China Soc. Mineral Petrol. Geochem. 39 (3), 8 (in Chinese with English abstract).
Li, Y.F., Zhang, T.W., Ellis, G.S., Shao, D.Y., 2017. Depositional environment and organic matter accumulation of upper ordovician-lower Silurian marine shale in the upper Yangtze platform, south China. Palaeogeogr. Palaeoclimatol. Palaeoecol. 466, 252–264.
Liu, S.J., Gao, G., Gang, W.Z., Xiang, B.L., Wang, M., Wang, C.Y., 2023a. Comparison of Formation Conditions of Source Rocks of Fengcheng and Lucaogou Formations in the Junggar Basin, NW China: Implications for Organic Matter Enrichment and Hydrocarbon Potential. J. Earth Sci. 34 (4), 1026–1040.
Liu, S.M., Jiang, L., Liu, B.J., Zhao, C.L., Tang, S.H., Tan, F.R., 2023b. Investigation of organic matter sources and depositional environment changes for terrestrial shale succession from the yuka depression: implications from organic geochemistry and petrological analyses. J. Earth Sci. 34 (5), 1–19.
Luning, S., Craig, J., Loydell, D.K., Storch, P., Fitches, B., 2000. Lower Silurian 'hot shales' in North Africa and Arabia: regional distribution and depositional model. Earth Sci. Rev. 49, 121–200.
Ma, Y.S., Chen, H.D., Wang, G.L., 2009. Atlas of Tectonic-Sequence Lithofacies Paleogeography in South China. Science Press, Beijing.
Ma, Y.Q., Fan, M.J., Lu, Y.C., Guo, X.S., Hu, H.Y., Chen, L., Wang, C., Liu, X.C., 2016. Geochemistry and sedimentology of the Lower Silurian Longmaxi mudstone in southwestern China: implications for depositional controls on organic matter accumulation. Mar. Petrol. Geol. 75, 291–309.
Mahoney, C., März, C., Buckman, J., Wagner, T., Blanco-velandia, V., 2019. Pyrite oxidation in shales: implications for palaeo-redox proxies based on geochemical and SEM-EDX evidence. Sediment. Geol. 389, 186–199.
Mansour, A., Wagreich, M., 2022. Earth system changes during the cooling greenhouse phase of the Late Cretaceous: coniacian-Santonian OAE3 subevents and fundamental variations in organic carbon deposition. Earth Sci. Rev. 229, 104022.
Mansour, A., Wagreich, M., Gentzis, T., Ocubalidet, S., Tahoun, S.S., Elewa, A.M., 2020. Depositional and organic carbon-controlled regimes during the Coniacian-Santonian event: first results from the southern Tethys (Egypt). Mar. Petrol. Geol. 115, 104285.
Mei, M.X., Ma, Y.S., Deng, J., Chu, H.M., Zheng, K.B., 2007. Sequence-stratigraphic frameworks and their palaeogeographic patterns for the Permian Lopingian of the Dianqiangui Basin and its adjacent areas of Southwestern China. Sci. China Earth Sci. 50, 869–885.
Mei, M.X., Maurice E, T., Wang, Y., Liu, M., 2013. Facies-succession and architecture of the third-order sequences and their stratigraphic framework of the Devonian in Yunnan-Guizhou-Guangxi area, South China. J. Palaeogeogr. 2, 93–108.
Neumeister, S., Algeo, T.J., Bechtel, A., Gawlick, H.J., Gratzer, R., Sachsenhofer, R.F., 2016. Redox conditions and depositional environment of the Lower Jurassic Bächental bituminous marls (Tyrol, Austria). Austrian Journal of Earth Sciences 109, 142–159.
Pan, J.N., Ge, T.Y., Liu, W.Q., Wang, K., Wang, X.L., Mou, P.W., Wu, W., Niu, Y.B., 2021. Organic matter provenance and accumulation of transitional facies coal and mudstone in Yangquan, China: insights from petrology and geochemistry. J. Nat. Gas Sci. Eng. 94, 104076.
Pan, X., Wang, Z., Li, Q., Gao, J., Zhu, L., Liu, W., 2020. Sedimentary environments and mechanism of organic matter enrichment of dark shales with low TOC in the Mesoproterozoic Cuizhuang Formation of the Ordos Basin: evidence from petrology, organic geochemistry, and major and trace elements. Mar. Petrol. Geol. 122, 104695.
Pedersen, T., Calvert, S.E., 1990. Anoxia vs. productivity: what controls the formation of organic-carbon-rich sediments and sedimentary rocks? AAPG (Am. Assoc. Pet. Geol.) Bull. 74 (4), 454–466.
Pickel, W., Kus, J., Flores, D., Kalaitzidis, S., Christanis, K., Cardott, B.J., Crosdale, P., 2017. Classification of liptinite-ICCP system 1994. Int. J. Coal Geol. 169, 40–61.
Playter, T.L., Konhauser, K., Owttrim, G., Hodgson, C., Warchola, T., Mloszewska, A.M., Sutherland, B., Bekker, A., Zonneveld, J.P., Pemberton, S.G., Gingras, M., 2017. Microbe-clay interactions as a mechanism for the preservation of organic matter and trace metal biosignatures in black shales. Chem. Geol. 459, 75–90.
Qie, W.K., Ma, X.P., Xu, H.H., Qiao, L., Liang, K., Guo, W., Song, J.J., Chen, B., Lu, J.F., 2019. Devonian integrative stratigraphy and timescale of China. Sci. China Earth Sci. 62, 112–134.
Qiu, Z., Liu, B., Lu, B., Shi, Z.S., Li, Z.Y., 2022. Mineralogical and petrographic characteristics of the Ordovician-Silurian Wufeng-Longmaxi Shale in the Sichuan Basin and implications for depositional conditions and diagenesis of black shales. Mar. Petrol. Geol. 135, 105428.
Raiswell, R., Berner, R.A., 1985. Pyrite formation in euxinic and semi-euxinic sediments. Am. J. Sci. 285, 710–724.
Raiswell, R., Berner, R.A., 1986. Pyrite and organic matter in Phanerozoic normal marine shales. Geochem. Cosmochim. Acta 50, 1967–1976.

Raiswell, R., Buckley, F., Berner, R.A., Anderson, T.F., 1988. Degree of pyritization of iron as a paleoenvironmental indicator of bottom-water oxygenation. J. Sediment. Petrol. 58, 812–819.
Ricken, W., 1996. Bedding rhythms and cyclic sequences as documented in organic carbon-carbonate patterns, Upper Cretaceous, Western Interior, US. Sediment. Geol. 102 (1–2), 131–154.
Rimmer, S.M., 2004. Geochemical paleoredox indicators in devonian-mississippian black shales, central Appalachian Basin (USA). Chem. Geol. 206, 373–391.
Ross, D.J.K., Bustin, R.M., 2009. Investigating the use of sedimentary geochemical proxies for paleoenvironment interpretation of thermally mature organic-rich strata: examples from the Devonian-Mississippian shales, Western Canadian Sedimentary Basin. Chem. Geol. 260, 1–19.
Rowe, H.D., Loucks, R.G., Ruppel, S.C., Rimmer, S.M., 2008. Mississippian Barnett formation, fort worth basin, Texas: Bulk geochemical inferences and Mo-TOC constraints on the severity of hydrographic restriction. Chem. Geol. 257, 16–25.
Schoepfer, S.D., Shen, J., Wei, H.Y., Tyson, R.V., Ingall, E., Algeo, T.J., 2015. Earth-Science Reviews Total organic carbon, organic phosphorus, and biogenic barium fluxes as proxies for paleomarine productivity. Earth Sci. Rev. 149, 23–52.
Schneider, W., Geng, A., Liu, X.Z., 1991. Diagenesis and mineralization processes in Devonian carbonate rocks of the Siding-Gudan lead-zinc mineral subdistrict, Guangxi, southwest China. Carbonates Evaporites 6, 53–68.
Scotese, C.R., 2001. Digital paleogeographic map archive on CD-ROM. In: PALEOMAP Project. University of Texas, Arlington. http://www.scotese.com (PALEOMAP website).
Scotese, C.R., McKerrow, W.S., 1990. Revised World maps and introduction. In: Palaeogeo-graphy and Biogeography, vol. 12. Geological Society Memoir, pp. 1–21.
Shao, T.B., Zhou, Y., Cai, Y.F., Liang, X.Q., Song, M.S., 2020. Detrital zircon U-Pb ages and Hf isotopes of Lower-Middle Devonian to Middle Jurassic sandstones in the Qinfang basin, southern South China block: constraints on provenance and tectonic setting. J. Asian Earth Sci. 204, 104578.
Singh, P., 2008. Lithofacies and Sequence Stratigraphic Framework of the Barnett Shale, Northeast Texas. University of Oklahoms, Norman, p. 181.
Summerhayes, C.P., 1987. Oceanography: an Illustrated Guide, vol. 23. Heyden & Son Ltd, California.
Sweere, T., van den Boorn, S., Dickson, A.J., Reichart, G.J., 2016. Definition of new trace-metal proxies for the controls on organic matter enrichment in marine sediments based on Mn, Co, Mo and Cd concentrations. Chem. Geol. 441, 235–245.
Tang, L., Song, Y., Jiang, S., Jiang, Z.X., Li, Z., Yang, Y.D., Li, X.H., Xiao, L., 2020. Organic matter accumulation of the Wufeng-Longmaxi shales in southern Sichuan Basin: evidence and insight from volcanism. Mar. Petrol. Geol. 120, 104564.
Taylor, S.R., Mclennan, S.M., 1985. The Continental Crust: its Composition and Evolution. Blackwell, London.
Teng, J., Mastalerz, M., Liu, B., 2021. Petrographic and chemical structure characteristics of amorphous organic matter in marine black shales: insights from Pennsylvanian and Devonian black shales in the Illinois Basin. Int. J. Coal Geol. 235, 103676.
Tribovillard, N.P., Algeo, T.J., Baudin, F., Riboulleau, A., 2012. Analysis of marine environmental conditions based on molybdenum-uranium covariation-Applications to Mesozoic paleoceanography. Chem. Geol. 324–325, 46–58.
Tribovillard, N.P., Algeo, T.J., Lyons, T., Riboulleau, A., 2006. Trace metals as paleoredox and paleoproductivity proxies: an update. Chem. Geol. 232, 12–32.
Tribovillard, N.P., Desprairies, A., Lallier-Vergès, E., Bertrand, P., Moureau, N., Ramdani, A., Ramanampisoa, L., 1994. Geochemical study of organic-matter rich cycles from the Kimmeridge Clay Formation of Yorkshire (UK): productivity versus anoxia. Palaeogeogr. Palaeoclimatol. Palaeoecol. 108 (1–2), 165–181.
Tyson, R.V., 1995. Sedimentary organic matter. In: Tyson, R.V. (Ed.), Organic Facies and Palynofacies. Chapman and Hall, London.
Walliser, O.H., 1996. Global events in the devonian and carboniferous. In: Global Events and Event Stratigraphy in the Phanerozoic: Results of the International Interdisciplinary Cooperation in the IGCP-Project 216 “Global Biological Events in Earth History”, vols. 225–250. Springer Berlin Heidelberg, Berlin, Heidelberg.
Wang, C.S., Wang, Z., Ye, Y.Q., Wu, J.Y., Li, Z.S., Tang, S.R., 2018. Structural evolution and its impact assessment on oil and gas reservoirs in Tianlin region, Guangxi. China Mining Magazine 27 (S1), 159–163.
Wang, N., Li, M.J., Tian, X.W., Hong, H.T., Wen, L., Wang, W.Z., 2020. Climate-ocean control on the depositional watermass conditions and organic matter enrichment in lower Cambrian black shale in the upper Yangtze Platform. Mar. Petrol. Geol. 120, 104570.
Wang, Q., Groves, D., 2018. Carlin-style gold deposits, Youjiang Basin, China: tectono-thermal and structural analogues of the Carlin-type gold deposits, Nevada, USA. Miner. Deposita 53, 909–918.
Wang, X.Q., Zhu, Y.M., Lash, G.G., Wang, Y., 2019. Multi-proxy analysis of organic matter accumulation in the Upper Ordovician-Lower Silurian black shale on the Upper Yangtze Platform, south China. Mar. Petrol. Geol. 103, 473–484.
Wei, H., Feng, Q.L., Yu, J.X., Chang, S., 2022. Characteristics and sources of organic matter from the early cambrian niutitang formtion and its preservation environment in Guizhou. J. Earth Sci. 33 (4), 933–944.
Wignall, P.B., Bond, D.P.G., Kuwahara, K., Kakuwa, Y., Newton, R.J., Poulton, S.W., 2010. An 80 million year oceanic redox history from Permian to Jurassic pelagic sediments of the Mino-Tamba terrane, SW Japan, and the origin of four mass extinctions. Global Planet. Change 71, 109–123.
Wignall, P.B., Newton, R., 1998. Pyrite framboid diameter as a measure of oxygen deficiency in ancient mudrocks. Am. J. Sci. 298 (7), 537–552.
Wilkin, R.T., Barnes, H.L., Brantley, S.L., 1996. The size distribution of framboidal pyrite in modern sediments: an indicator of redox conditions. Geochem. Cosmochim. Acta 60 (20), 3897–3912.
Wilkin, R.T., Barnes, H.L., 1997. Formation processes of framboidal pyrite. Geochem. Cosmochim. Acta 61 (2), 323–339.
Wu, J., Liang, C., Hu, Z.Q., Yang, R.C., Xie, J., Wang, R.Y., Zhao, J.H., 2019. Sedimentation mechanisms and enrichment of organic matter in the ordovician Wufeng formation-Silurian Longmaxi Formation in the Sichuan Basin. Mar. Petrol. Geol. 101, 556–565.
Wu, L.Y., Hu, D.F., Lu, Y.C., Liu, R.B., Liu, X.F., 2016. Advantageous shale lithofacies of Wufeng formation-longmaxi Formation in fuling gas field of Sichuan Basin, SW China. Petrol. Explor. Dev. 43, 208–217.
Wu, Y.B., Feng, Q., Gong, Y.M., 2013. Blooming of bacteria and algae is a biokiller for mass-extinction of Devonian coral-stromatoporoid reef ecosystems. Sci. China Earth Sci. 43, 1156–1167.
Wu, Y.W., Tian, H., Gong, D.J., Li, T.F., Zhou, Q., 2020. Paleo-environmental variation and its control on organic matter enrichment of black shales from shallow shelf to slope regions on the Upper Yangtze Platform during Cambrian Stage 3. Palaeogeogr. Palaeoclimatol. Palaeoecol. 545, 109653.
Wu, Y.W., Tian, H., Li, T.F., Ji, S., Liu, Z.Y., Xiao, X.M., Xie, L.H., 2021. Enhanced terrestrial organic matter burial in the marine shales of Yangtze platform during the early Carboniferous interglacial interval. Mar. Petrol. Geol. 129, 105064.
Wu, Y.W., Tian, H., Liu, Z.Y., Liu, S.L., Li, T.F., Ji, S., Peng, P.A., 2022. Interpretation of abnormally negative carbon isotope excursions in Eifelian–Givetian (Middle Devonian) sediments of South China and implications for paleo-environmental variation. Palaeogeogr. Palaeoclimatol. Palaeoecol. 604, 111225.
Xiao, B., Liu, S.G., Li, Z.W., Ran, B., Ye, Y.H., Yang, D., Li, J.X., 2021. Geochemical characteristics of marine shale in the Wufeng Formation-Longmaxi Formation in the northern Sichuan Basin, South China and its implications for depositional controls on organic matter. J. Petrol. Sci. Eng. 203, 108618.
Yan, C.N., Jin, Z.J., Zhao, J.H., Du, W., Liu, Q.Y., 2018. Influence of sedimentary environment on organic matter enrichment in shale: a case study of the Wufeng and Longmaxi Formations of the Sichuan Basin, China. Mar. Petrol. Geol. 92, 880–894.
Yang, J., Du, Y.S., Huang, H., Yang, J.H., Huang, H.W., Huang, Z.Q., 2023. Devonian-carboniferous pillow OIB-type Basalts in the Youjiang Basin, SW China: implications for the eastern extension of the paleo-tethys Branch ocean. J. Earth Sci. 34 (3), 690–705.
Yang, L., Deng, J., Groves, D.I., Wang, Q.F., Zhang, L., Wu, W., Qin, K., Zhang, Q.Z., 2020. Recognition of two contrasting structural- and mineralogical-gold mineral systems in the Youjiang basin, China-Vietnam: orogenic gold in the south and Carlin-type in the North. Geosci. Front. 11, 1477–1494.
Yu, C.M., Qie, W.K., Lu, J.F., 2018. Emsian (early devonian) yujiang event in southsouth China. Palaeoworld 27, 53–65.
Yuan, K., Huang, W.H., Fang, X.X., Li, S.Z., Wang, T., Lin, T., Liu, G.H., 2020. Geochemical characteristics and sedimentary environment of the middle devonian organic-rich shales in the northwest of guizhong depression, southwest China. China Geology 3, 567–574.
Zhang, B., Yan, D.T., Drawarh, H.J., Yang, X.R., He, J., Zhang, L.W., 2020. Formation mechanism and numerical model of quartz in fine-grained organic-rich shales: a case study of Wufeng and longmaxi Formations in western hubei Province, south China. J. Earth Sci. 31 (2), 354–367.
Zhang, G.Y., Tong, X.G., Xin, R.C., Wen, Z.X., Ma, F., Huang, T.F., Wang, Z.M., Yu, B.S., Li, Y.J., Chen, H.L., Liu, X.B., Liu, Z.D., 2019. Evolution of lithofacies and paleogeography and hydrocarbon distribution worldwide (I). Petrol. Explor. Dev. 46, 664–686.
Zhao, C.J., Jiang, Y.L., Yang, H.X., Wang, L.J., 2022. The genesis of authigenic minerals and the porosity evolution of various lithologies and their implication for identifying high-quality reservoirs in the fourth member of Xujiahe Formation (Northeast-Sichuan Basin, China). J. Petrol. Sci. Eng. 212, 110261.
Zheng, S.C., Feng, Q.L., van de Velde, S., Chang, S., Zhang, L., Gao, B., 2022. Microfossil assemblages and indication of the source and preservation pattern of organic matter from the early cambrian in southsouth China. J. Earth Sci. 33 (3), 802–819.
Zhou, Q.X., Liu, Y.X., Li, T., Zhao, H.Z., Alessi, D.S., Liu, W.T., Konhauser, K.O., 2020. Cadmium adsorption to clay-microbe aggregates: implications for marine heavy metal cycling. Geochem. Cosmochim. Acta 290, 124–136.
Zhong, N.N., Lu, S.F., Huang, Z.L., Zhang, Y.S., 2004. TOC changes in the process of thermal evolution of source rock and its controls. Science in China 47 (S2), 141–149.
Zou, C.N., Yang, Z., Zhang, G.S., Zhu, R.K., Tao, S.Z., Yuan, X.J., Hou, L.H., Dong, D.Z., Guo, Q.L., Song, Y., Ran, Q.Q., Wu, S.T., Ma, F., Bai, B., Wang, L., Xiong, B., Pan, S. Q., Liu, H.L., Wang, X.N., 2023. Theory, technology and practice of unconventional petroleum geology. J. Earth Sci. 34 (4), 951–965.
Zou, C.N., Zhu, R.K., Chen, Z.Q., Ogg, J.G., Wu, S.T., Dong, D.Z., Qin, Z., Wang, Y.M., Wang, L., Lin, S.H., Cui, J.W., Su, L., Yang, Z., 2019. Organic-matter-rich shales of China. Earth Sci. Rev. 189, 51–78.